

**POWER COMPOSITES:
STRUCTURAL MATERIALS THAT GENERATE
AND STORE ELECTRICAL ENERGY**

Final Report

Prepared by:

Donald A. Shockey, Associate Director, Materials Research Lab
Susanna C. Ventura, Associate Director, Product Development Center
Subhash C. Narang, Director, Product Development Center
Jeffrey W. Simons, Sr. Computational Mech., Materials Research Lab
Benjamin C. Bourne, Research Engineer, Poulter Lab
Brian D. Peterson, Research Engineer, Materials Research Lab
Physical Sciences Division

SRI International
333 Ravenswood Avenue
Menlo Park, CA 94025-3493

October 31, 2005

U.S. ARMY RESEARCH OFFICE
Contract Number DAAD19-00-C-0098

APPROVED FOR PUBLIC RELEASE;
DISTRIBUTION UNLIMITED

Report Documentation Page				Form Approved OMB No. 0704-0188	
Public reporting burden for the collection of information is estimated to average 1 hour per response, including the time for reviewing instructions, searching existing data sources, gathering and maintaining the data needed, and completing and reviewing the collection of information. Send comments regarding this burden estimate or any other aspect of this collection of information, including suggestions for reducing this burden, to Washington Headquarters Services, Directorate for Information Operations and Reports, 1215 Jefferson Davis Highway, Suite 1204, Arlington VA 22202-4302. Respondents should be aware that notwithstanding any other provision of law, no person shall be subject to a penalty for failing to comply with a collection of information if it does not display a currently valid OMB control number.					
1. REPORT DATE 31 MAY 2006		2. REPORT TYPE N/A		3. DATES COVERED -	
4. TITLE AND SUBTITLE Power Composites: Structural Materials that Generate and Store Electrical Energy				5a. CONTRACT NUMBER	
				5b. GRANT NUMBER	
				5c. PROGRAM ELEMENT NUMBER	
6. AUTHOR(S)				5d. PROJECT NUMBER	
				5e. TASK NUMBER	
				5f. WORK UNIT NUMBER	
7. PERFORMING ORGANIZATION NAME(S) AND ADDRESS(ES) SRI International 333 Ravenswood Avenue Menlo Park, CA 94025				8. PERFORMING ORGANIZATION REPORT NUMBER	
9. SPONSORING/MONITORING AGENCY NAME(S) AND ADDRESS(ES)				10. SPONSOR/MONITOR'S ACRONYM(S)	
				11. SPONSOR/MONITOR'S REPORT NUMBER(S)	
12. DISTRIBUTION/AVAILABILITY STATEMENT Approved for public release, distribution unlimited					
13. SUPPLEMENTARY NOTES The original document contains color images.					
14. ABSTRACT					
15. SUBJECT TERMS					
16. SECURITY CLASSIFICATION OF:			17. LIMITATION OF ABSTRACT SAR	18. NUMBER OF PAGES 43	19a. NAME OF RESPONSIBLE PERSON
a. REPORT unclassified	b. ABSTRACT unclassified	c. THIS PAGE unclassified			

CONTENTS

TABLE OF FIGURES	3
EXECUTIVE SUMMARY	5
THE POWER COMPOSITE CONCEPT	7
FIBER BATTERY DEVELOPMENT	8
ENERGY HARVESTING FUNCTION	11
Piezo Tube Selection and Preparation	12
MECHANICAL BEHAVIOR	15
Four-Point Bend Tests	15
RULES AND TOOLS APPLICATION	19
Application Details	19
Web Applications.....	23
Future Work	27
FINITE ELEMENT CALCULATIONS	28
Approach.....	28
MODEL CALIBRATION	31
Bender Design: PZT/Aluminum Sandwich Beam.....	31
Experimental Setup.....	33
Bender Performance.....	34
Model Performance.....	36
MODEL DEMONSTRATION AND VALIDATION	37
Bender Design: Carbon Composite/PZT Tube Beam.....	37
Bender Performance.....	39
Model Performance.....	40
BENDER-BATTERY INTERACTION.....	40
DISCUSSION AND FUTURE WORK.....	42
REFERENCES	43

TABLE OF FIGURES

Figure 1. Schematic of the power composite. The material generates, stores, and delivers electrical energy while providing structural strength and stiffness	5
Figure 2. Schematic of the self-sustaining power composite concept.	7
Figure 3. Battery construction.....	8
Figure 4. Schematic of the battery fabrication process.....	8
Figure 5. Illustration of the microcapillary battery.....	10
Figure 6. Photograph of the microcapillary battery.....	10
Figure 7. Cycling properties of a filament battery encapsulated in a microcapillary with an internal diameter of 530 μm	11
Figure 8. Voltage production in a 3-1 PZT flat plate.....	11
Figure 9. Piezo tube (1.15-mm-OD, 0.650-mm-ID).....	12
Figure 10. Process for coating inside wall of PZT tube with electroless copper.....	14
Figure 11. Piezo tube with (above) and without (below) copper plating.....	14
Figure 12. Process for coating inside wall of PZT tube with electroless copper.....	15
Figure 13. Battery fiber configurations in composite laminate plates.....	17
Figure 14. Maximum stress versus displacement in four-point-bend.....	18
Figure 15. Bimorph size constraints.	20
Figure 16. Natural Frequency Calculator.....	23
Figure 17. Screen shot of bending response tool.	25
Figure 18. Input motion for vibration with 5% damping (A) and 40% damping (B).....	25
Figure 19. Tip response with 5% damping (A) and 40% damping (B).	26
Figure 20. Vibration-charged battery design tool.	27
Figure 21. Range of composite thicknesses and beam lengths that yield the desired resonant frequency.....	27
Figure 22. Cross-sectional and top view schematics of the 3-layer PZT/Aluminum sandwich beam (not to scale).	32
Figure 23. Photo of the 3-layer PZT/aluminum sandwich beam.	33
Figure 24. Photograph of the experimental setup.	33
Figure 25. Photograph of the vibration test rig.	34
Figure 26. Free vibration response of the PZT/aluminum sandwich beam.	35
Figure 27. Tip displacement and piezo voltage output for a given sinusoidal base displacement of the PZT/aluminum sandwich beam at 525 Hz.	35
Figure 28. Measured and calculated tip displacement for the PZT/aluminum sandwich beam. ..	36

Figure 29. Measured and calculated voltage output for the PZT/aluminum sandwich beam.....	37
Figure 30. Schematic of carbon fiber/PZT tube/epoxy matrix sandwich beam.	38
Figure 31. Photos of fabricated carbon fiber/PZT/epoxy matrix sandwich beam.	38
Figure 32. Measured tip displacement and output voltage for the PZT tube beam.	39
Figure 33. Measured and calculated tip displacement and output voltage for the PZT tube beam.	40
Figure 34. Voltage, current, and power output for the PZT tube beam.	41
Figure 35. Lithium-ion battery charge and discharge curves.	41
Figure 36. Fiber battery inserted into PZT tube.....	42

EXECUTIVE SUMMARY

We describe progress in the development of a synthetic multifunctional material: namely a fiber composite with both power and structural function. The structural composite contains batteries encased in piezoelectric tubes. When the structure vibrates the tubes generate electricity that is stored in the batteries; thus the composite material provides a long-term and stable self-recharging source of power that can be used, for example, to drive electronics. We also developed an analytic model to facilitate the design of power composites for specific DoD applications.

The approach as illustrated in Figure 1 was to produce **battery fibers** that can store and deliver electrical energy, insert them into hollow **piezoelectric fibers** that provide structure and can harvest mechanical energy and charge the battery fibers, and incorporate them in a **polymer matrix** along with additional **structural fibers** that increase the load-carrying capability. The

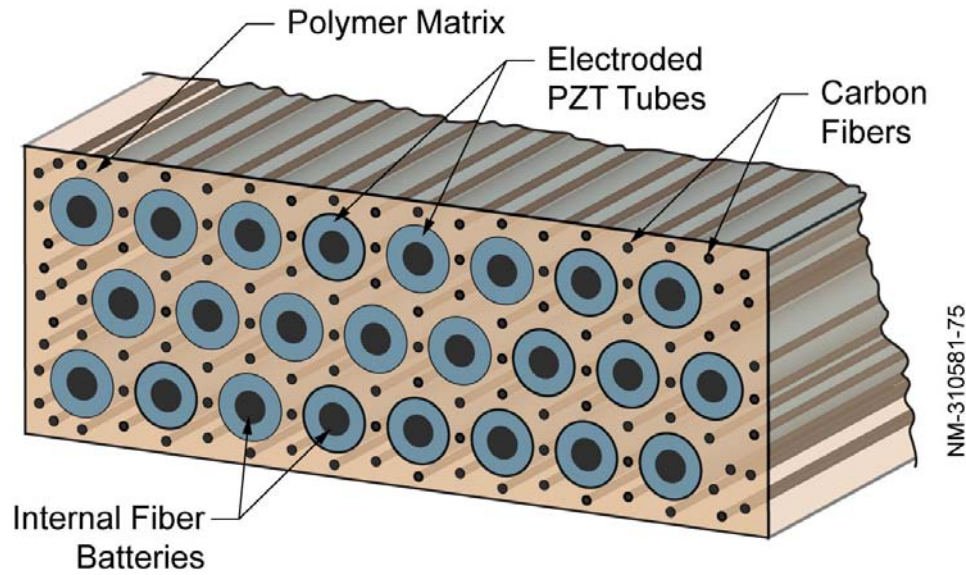


Figure 1. Schematic of the power composite. The material generates, stores, and delivers electrical energy while providing structural strength and stiffness

fiber batteries were fabricated by coating 7-mil diameter carbon fibers with LiCoO_2 cathode material in a scalable, low-cost dip process and coupling them with bare carbon fiber anode fibers. The batteries were characterized with regard to energy, power, and cycle life.

An energy harvesting function was achieved with 400- μm -diameter piezoelectric tubes, which convert mechanical (vibrational) energy to electrical energy. By combining the PZT tubes with the fiber batteries, we demonstrated the self-recharging attribute of the power composite (no requirement for external wires or periodic removal for recharging batteries).

The battery fibers are inserted in the hollow PZT fibers creating power fibers that will be embedded in the polymer matrix using commercial manufacturing processes. If needed, strength

and stiffness of the polymer matrix will be enhanced by conventional structural fibers that are incorporated along with the power fibers.

We developed an analytical model that can guide power composite design. Used alone or as part of an expert system, the web-based-MATLAB program computes the number and spatial distribution of the three fiber types (battery, PZT, and structural) necessary to meet the power and structural requirements of a given application.

This report summarizes the procedures and results of the fiber battery properties and processing work and describes in detail the energy harvesting characterization. Details of the fiber battery development and the analytical modeling are given in previous progress reports, References 1 and 2.

The practicality of the power composite material described here is promising. The material can be designed so that mechanical and power functions can be traded off to fit particular applications, and promises to be producible by low-cost, scalable, and existing manufacturing procedures. Potential applications include morphing aircraft wings and powering remote or embedded diagnostic and RF sensors and transmitters. Additional effort is needed to produce and evaluate the performance of prototype specimens.

THE POWER COMPOSITE CONCEPT

In seeking to develop a structural material having a self-sustaining power source for driving remote and/or inaccessible low-energy sensors and devices, we used existing and new technologies at SRI to design a multifunctional material—a power composite that can generate, store, and deliver electrical power while providing structural function. Figure 2 shows the conceptual material, which consists of fiber batteries within hollow piezoceramic fibers embedded in a polymer matrix along with structural fibers. When the structure vibrates, the tubes generate electrical power that is conditioned and stored in the fiber batteries. The self-charging batteries provide a long-term and stable power supply for driving electronics.

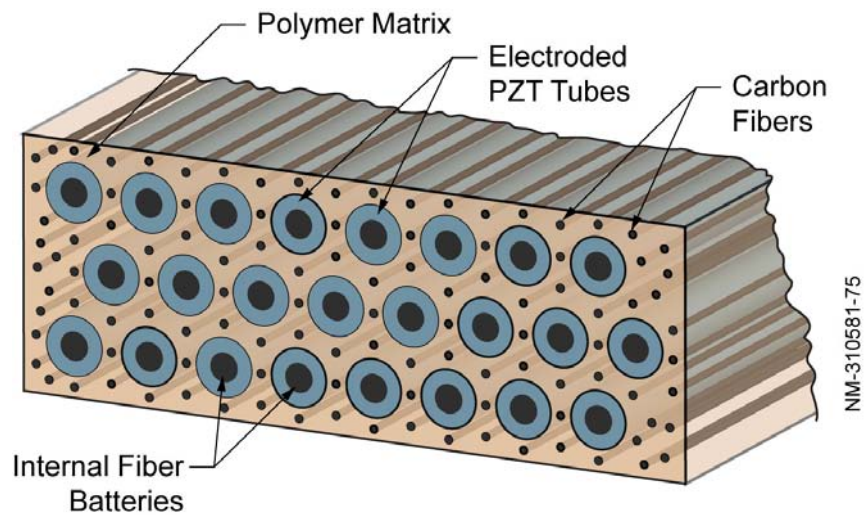


Figure 2. Schematic of the self-sustaining power composite concept.

In the following sections of this report we describe our efforts to develop and characterize fiber batteries; acquire, characterize, and couple hollow piezoceramic fibers to the batteries; make and test mechanical performance of power composites; and develop a computational program for designing power composites for specific DoD applications.

FIBER BATTERY DEVELOPMENT

Batteries were made from commercially available, high-strength carbon fibers. The fibers served as the electrode/current collector for the battery. The components are shown in Figure 3.

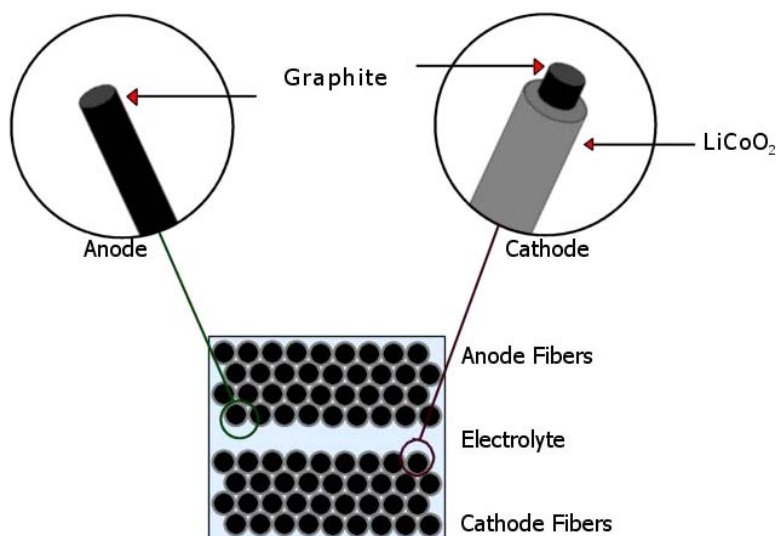


Figure 3. Battery construction.

The lithium ion fiber battery is fabricated exclusively by solution-based processes, such as dip-coating. The anode fiber tow and the cathode fiber tow are separately fabricated, coated by a polymer electrolyte layer, and laminated into a monolithic battery fiber tow. Figure 4 is a schematic of the fabrication process.

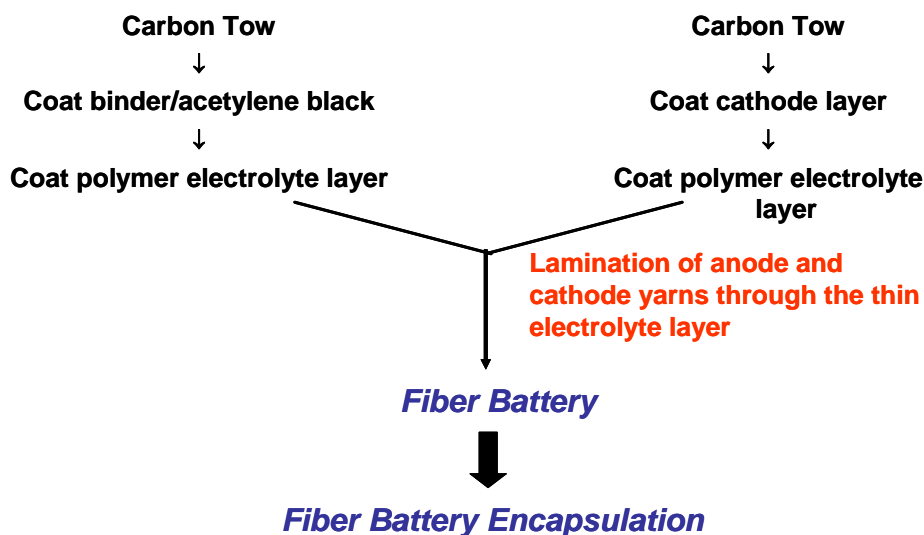


Figure 4. Schematic of the battery fabrication process.

PAN-based carbon fibers are preferred for the anode because they can be handled more readily than pitch-based carbon fibers and offer the best combination of mechanical properties and lithium intercalation capacity. PAN-based T650/35 carbon fibers that were pretreated by soaking at 400°C for 8 hours under argon were found to have a discharge capacity of 248 mAh/g.

Carbon fiber tows were also used as cathode current collectors. Lithium cobalt oxide was used as the cathode active material because of its high current capacity (148 Ah/g) and excellent reversibility. The carbon fiber cathodes were fabricated by coating a carbon fiber with a dispersion of lithium cobalt oxide, acetylene black, and polymer binder.

Both anode fiber and cathode carbon tows were first coated with a separator consisting of a polymer binder and submicron silica powder, and then laminated together. The battery is activated by addition of a liquid electrolyte to the porous separator.

The battery needs to be encapsulated to protect it from the degrading effects of moisture and air. In typical commercial lithium polymer batteries, the battery encapsulant is a laminate consisting of multiple layers of aluminum and polymer. We have tested several encapsulant materials, including hydrophobic epoxies activated by low-temperature initiators, photocurable epoxies, and vinyl ester. However, we found that these encapsulants had limited efficacy.

We have recently shown the feasibility of encapsulating fiber batteries into silica microcapillaries of the kind typically used as columns in gas chromatography. These capillary tubes are available in a wide range of inner and outer diameters and wall thicknesses. We have typically used glass microcapillaries with an inner diameter (ID) of 697 μm or 532 μm and an outer diameter (OD) of 850 μm or 662 μm , respectively. It should be noted that glass microcapillaries are available with ODs as small as 90 μm with a wall thickness of 35 μm (ID is 20 μm). The microcapillaries are quite flexible because they are coated with a thin layer of polyimide. In these batteries we typically use a few carbon fibers coated by a dispersion of acetylene black in a polymer binder as the anode. A copper wire (25- μm diameter) is placed in contact with the carbon fibers to facilitate current collection. The cathode is constituted by a small number of carbon fibers (~50-100) coated by a dispersion of lithium cobalt oxide and acetylene black in a polymer binder (i.e., polyvinylidene fluoride, or PVDF). The separator, a thin layer of a dispersion of silica in polysiloxane and PVDF, is typically applied on the cathode filament.

The anode and copper wire are inserted first, followed by the cathode filament. Typically both anode and cathode leads come out from the same side of the capillary. After sealing one of the microcapillary tips with epoxy, the liquid electrolyte is added into the capillary by vacuum filling. The electrical leads which pass through the other microcapillary tip are sealed using a small heat-shrinking tube. Figure 5 show a schematic illustration and Figure 6 shows a photograph of the microcapillary battery, respectively.

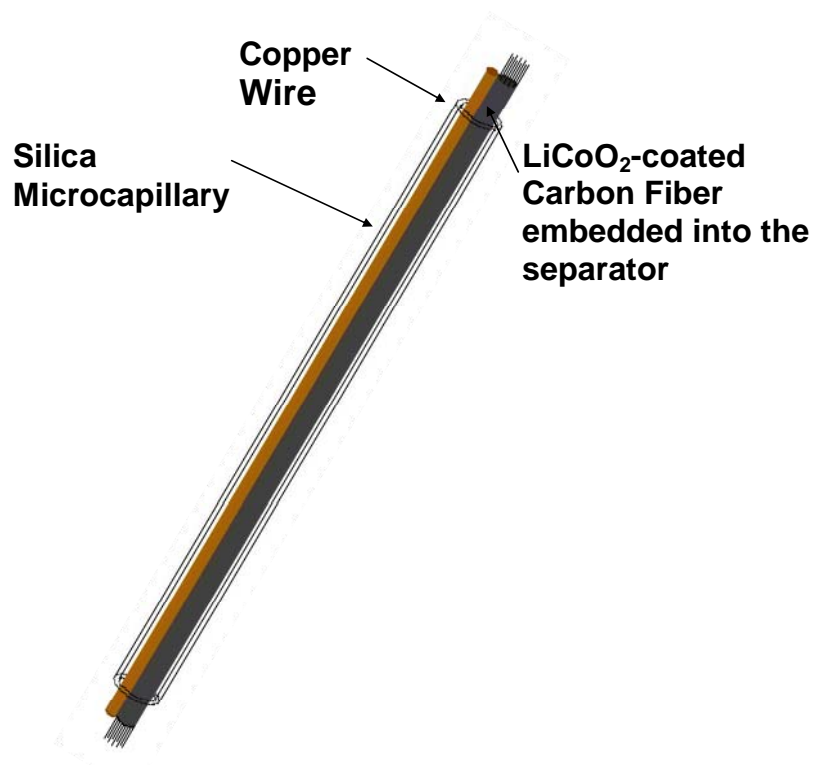


Figure 5. Illustration of the microcapillary battery.

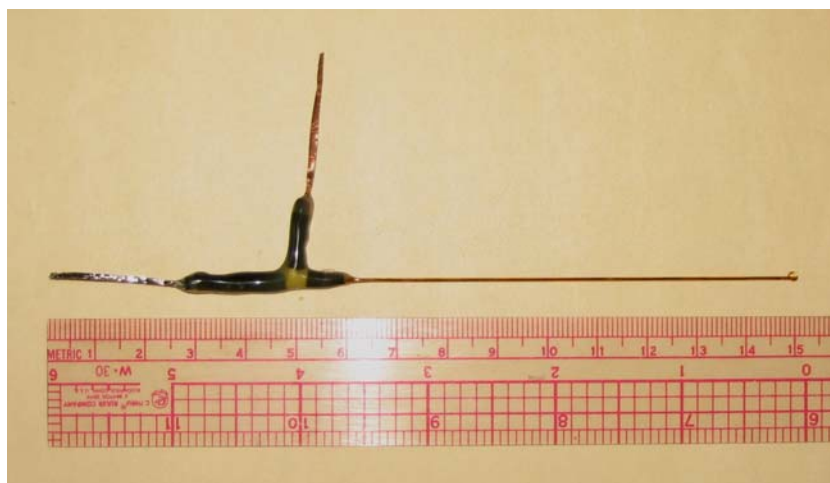


Figure 6. Photograph of the microcapillary battery.

Figure 7 illustrates the cycling properties of a 5-cm filament battery encapsulated in a microcapillary with an internal diameter of 530 μm . The battery is charged at 0.060 mA and discharged at 0.120 mA. At this rate the battery capacity is 0.2 mAh.

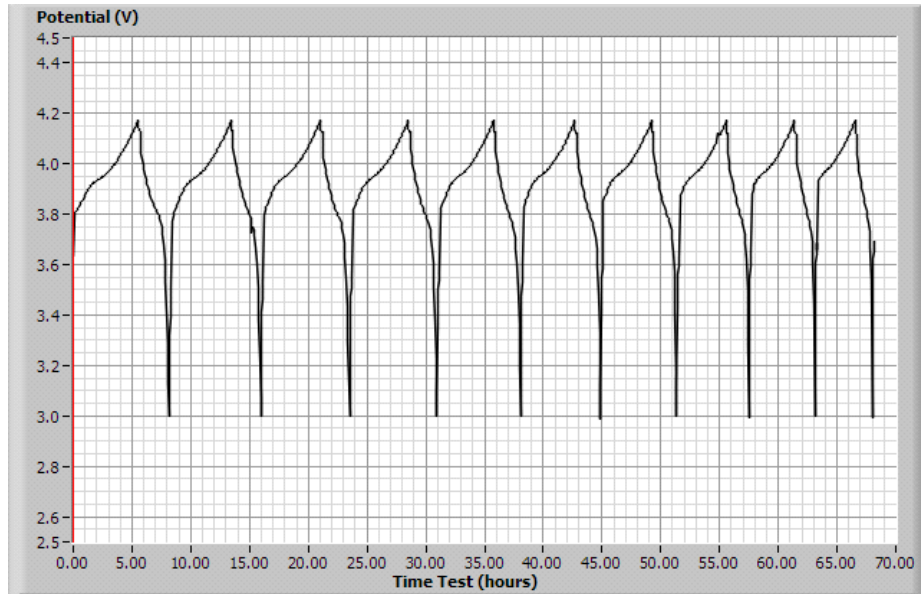


Figure 7. Cycling properties of a filament battery encapsulated in a microcapillary with an internal diameter of 530 μm .

ENERGY HARVESTING FUNCTION

We used lead zirconium titanate (PZT) piezoelectric material to achieve an energy harvesting function. We envisioned inserting the fiber batteries into hollow PZT tubes about 400 microns in diameter and connecting them electrically to store converted vibrational energy. Flat PZT plates are already used extensively for power generation and motor function. Figure 8 illustrates the voltage potential that develops between electrodes on the upper and lower plate surfaces when transverse loads are applied to the structure.

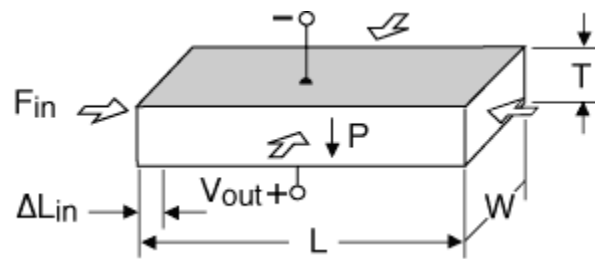


Figure 8. Voltage production in a 3-1 PZT flat plate.

The strain-induced voltage characteristics of these piezoceramics are well understood and documented. A typical piezoelectric sheet can be treated as a parallel plate capacitor whose capacitance is given by

$$C_p = \frac{e_{33}Lw}{th}$$

where e_{33} is the relative permittivity of the piezoceramic material and L , w and th are the length, width, and thickness of the piezo generator, respectively. Considering the effect of strain only along the length of the beam (1-direction), the voltage generated by the sensor can be expressed as

$$V = \frac{d_{31}Ew}{C_p} \varepsilon_1^*$$

where d_{31} and E are the piezoceramic charge constant and Young's modulus, respectively, and ε_1^* is an averaged strain across the sheet. This averaged strain is calculated as a fraction of the maximum strain in the material for nonuniform loading (e.g., bending of a cantilevered beam).

Piezo Tube Selection and Preparation

Techniques currently exist for using rigid PZT fibers in rigid power structures and flexible carbon fibers in flexible power structures. These structures generate voltage across the fiber diameter by placing opposing leads on the upper and lower surfaces along the length of the fibers.

Our proposed power fiber requires that PZT fibers be electroded on both the outer and inner wall surfaces. When strained axially along the length of the tube, a voltage potential is produced across the wall thickness. Several manufacturers currently distribute pre-plated and poled tubes, but with limited lengths ranging from approximately 2-40 mm. For compatibility with our batteries we require tubes with cross-sectional dimensions of approximately 700 μm ID and 1.1 mm OD, and with lengths greater than 70 mm. To our knowledge, there are no commercially-available off-the-shelf PZT tubes that meet the above criteria. As shown in Figure 9, we chose a 0.650-mm-ID, 1.150-mm-OD and 150-mm-long PZT 5A1 tube produced by Smart Material Corporation (Osprey, FL).



Figure 9. Piezo tube (1.15-mm-OD, 0.650-mm-ID).

We selected the Smart Material fibers for their excellent dimensional uniformity along the length and through the wall thickness of each tube. While these tubes meet the quality and dimensional requirements for this application¹, they were neither electroded nor poled at the factory. Both the inner and outer wall surfaces must be coated with a conductive metallic surface to allow the voltage potential across the thickness of the tube. Furthermore, any piezoelectric material must be properly poled (the process of applying a large current between the metallized surfaces of the ceramic) to achieve the strain-voltage characteristic. We developed a suitable technique, discussed below, for electroding the inner and outer wall surfaces of the tubes and poling the metallized tubes.

Electroding Procedure. Two chelants (0.293 g of glycolic acid and 0.362 g of glyoxylic acid) were dissolved in 10 ml methanol. Palladium (II) acetate was suspended in 5 ml methanol in a round-bottom flask and mixed with a stir bar. The solution of mixed chelants was added to the palladium (II) acetate suspension in methanol drop by drop over a period of approximately 30 min. The round-bottom flask was purged with argon and wrapped with aluminum foil, and the contents were agitated for 3 hours at room temperature. A reddish solution resulted, and the contents of the flask were further stirred overnight at room temperature². The ingredients used in this process are all commercially available.

The PZT tubes were checked for dimensional compatibility with the polyimide battery insert (i.e., greater than 650 μm ID). The tubes found to be compatible for battery insertion were plated with copper electrodes using the catalytic palladium prepared above.

The palladium ink was filtered through a 0.45- μm filter. The inner surface of each tube was coated by pushing the solution of the palladium ink through a hypodermic syringe, as shown in Figure 10. The outer surface was coated by dipping the tubes in the solution. The PZT tubes were heated over a hot air gun while blowing air through each of them to coat with palladium internally as well as externally. This resulted in depositing catalytic palladium on the inner and outer surfaces of the PZT tubes.

A stock solution of the electroless formulation containing copper (II) nitrate, sodium hydroxide, sodium bicarbonate and Rochelle salt was prepared. We added 50 ml of 37% formaldehyde to 500 mm of this solution to get the electroless copper solution. The setup for electroless coating is shown in Figure 10 and a coated tube is shown in Figure 11.

¹ Smart Materials indicates that their tubes may not achieve full bulk material properties due to inconsistencies that develop during the fabrication process. The value of the potential reduction in voltage output estimate is documented as 65-75% of typical bulk material output.

² This method and formulation has been adapted from the U.S. Patent (5894038)

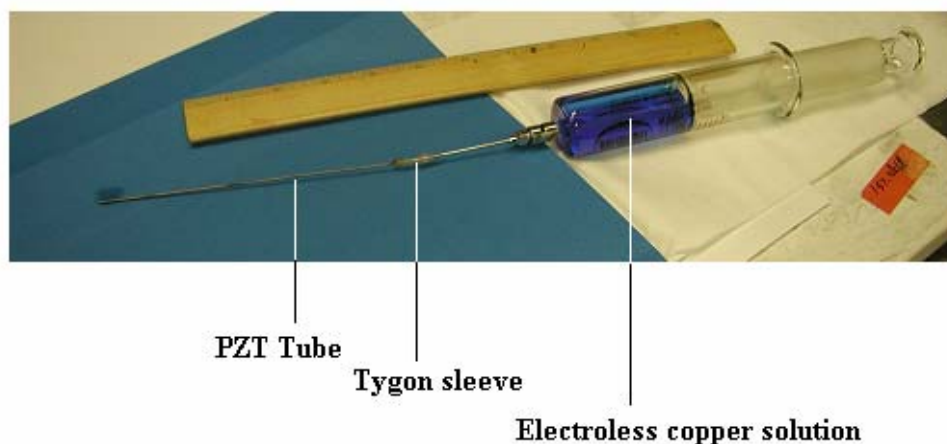


Figure 10. Process for coating inside wall of PZT tube with electroless copper.



Figure 11. Piezo tube with (above) and without (below) copper plating.

Poling Procedure. Following electroding, each tube was electrically poled to establish the piezo properties in the 3-1 direction. A thin copper wire was attached inside the PZT tube and a small copper clamp was attached to the outside surface. The PZT tube was filled with paraffin oil and immersed in an oil bath. The temperature of the oil bath was gradually increased to 120°C. A 500 VDC bias was applied across the two copper leads for 10 min. The PZT tube was then removed from the oil bath and cleaned to remove all residual oil. The poling of the PZT tube was verified by connecting to a signal generator and checking the strain response of the tube. Figure 12 shows a sketch of the poling setup.

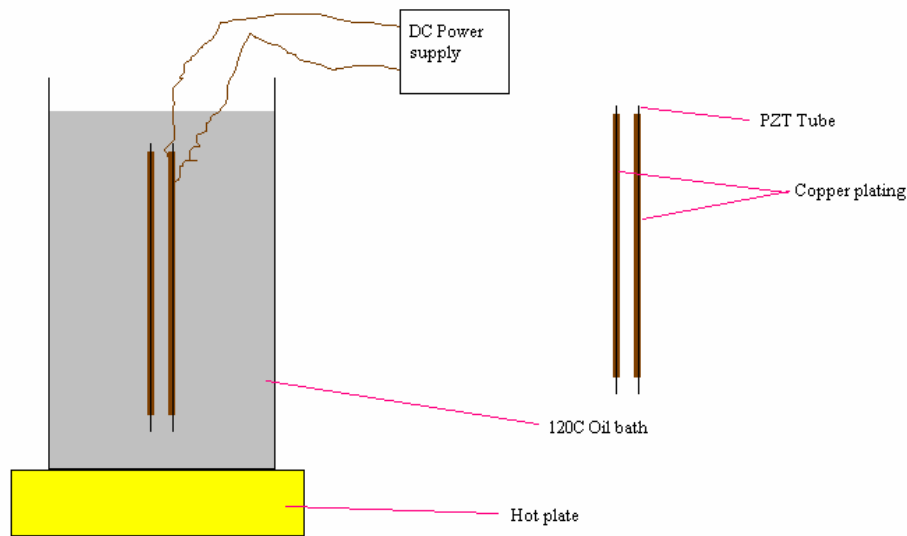


Figure 12. Process for coating inside wall of PZT tube with electroless copper.

MECHANICAL BEHAVIOR

Mechanical testing was done at both the micro and macro level to determine Young's Modulus, yield strength, post-yield stress-strain behavior, shear strength, and interface strength of composite plates. Properties of both power and standard composite plates and structures were measured in macro-level three-, and four-point-bend tests. These tests showed the effects of battery fiber tows and patches on structural response and the effects of loading on battery performance. The resulting material property data were used in detailed finite element analyses and to develop material design rules. Other mechanical tests indicated the effects of stress on the power function of the battery. The three-point-bend tests are described in 2002 Interim Progress Report. The four-point-bend tests are described below.

Four-Point Bend Tests

The series of four-point-bend tests on composite plates summarized in Table 1 showed the effect of battery encapsulation method. All plates were constructed from three layers of SikaWrap 103c unidirectional carbon fiber cloth, the properties of which are given in Table 2. The encapsulant was a polypropylene tape lay up and Epon 862/Epicure 3234 was the epoxy-resin system. The batteries and/or encapsulating tape were placed on the center layer and within this layer. The battery fiber tows were inserted slightly offset from the neutral axis of the cloth in an alternating pattern in either a dense or sparse configuration, Figure 13.

Table 1. Plates used in 4-pt-bend tests.

Plate No.	Details	Tape and/or Battery Configuration	Section Modulus (in ³)
T01	No batteries, vacuum bagged	None	0.003812
T02	No batteries, pressed	None	0.003938
T03	Tape only, no batteries	Two pieces of tape	0.003992
T04	Tape and batteries, pressed	Two tape encapsulated batteries	0.004476
T05	Roughed tape and batteries, pressed	Two pieces of tape	0.004177
T06	Tape only	Five pieces of tape	0.004402
T07	Tape with single sided cellophane	Five pieces of tape	0.004244
T08	Tape with double sided cellophane	Four pieces of tape	0.004095
129	Tape only	Seven pieces of tape	0.004557
130	Tape with DS VR5321	Five pieces of tape	0.006075

Table 2. Published properties for materials used in composite laminates.

Material	Density (g/cc)	Tensile Modulus (psi)	Tensile Strength (psi)
Sika Wrap Hex 103 C	1.8	34×10^6	550,000
Epi-Cure 3224/Epon 862	1.23	470×10^3	12,000

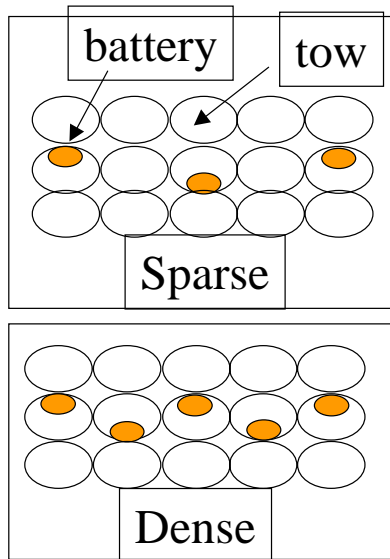


Figure 13. Battery fiber configurations in composite laminate plates.

Plate T01 was made using a vacuum bag technique. The plies were impregnated with epoxy and laid up on a metal plate. The plate was then sealed in a vacuum bag, so that one side of the composite was on the metal plate and one side was against the vacuum bag. As a result of this technique, the plates ended up with a slightly lenticular cross section, where the center of the plate was thicker than the edges.

The other plates were made using a press technique. These plates were placed in a form and pressed to maintain a uniform thickness across the entire length and width of the plate. The form was constructed such that the plates would be 4 in. wide by 0.087 in. thick.

The four-point bend tests used 0.5-in. diameter pins, with a bottom pin spacing of 4.33 in. and the top pins spaced 2.36 in. apart. The plates were loaded by moving the bottom pins upward at a constant rate of 0.001 in/min. Displacement and load were measured until plate failure.

Results are shown in Figure 14 as the maximum stress in the plate versus the displacement of the crosshead. Using the maximum stress, comparisons can easily be made between plates with different geometries.

In all cases except Plate 130, the slope of the stress/displacement curve is linear until yielding occurs. The plates without batteries achieve higher peak stresses than those with batteries, a trend found in all the plates tested. As the number of batteries and/or tape is increased, the slope of the stress/displacement curve and the failure strength decreases. For the plates with two pieces of tape only, or two encapsulated batteries, the slopes and peak stresses are nearly identical. This trend indicates that the addition of batteries into the tape, or the roughing of the tape, has little effect on the mechanical properties. A similar trend is found when five pieces of tape were tested, with single and double sided cellophane added to the outside of the polypropylene tape.

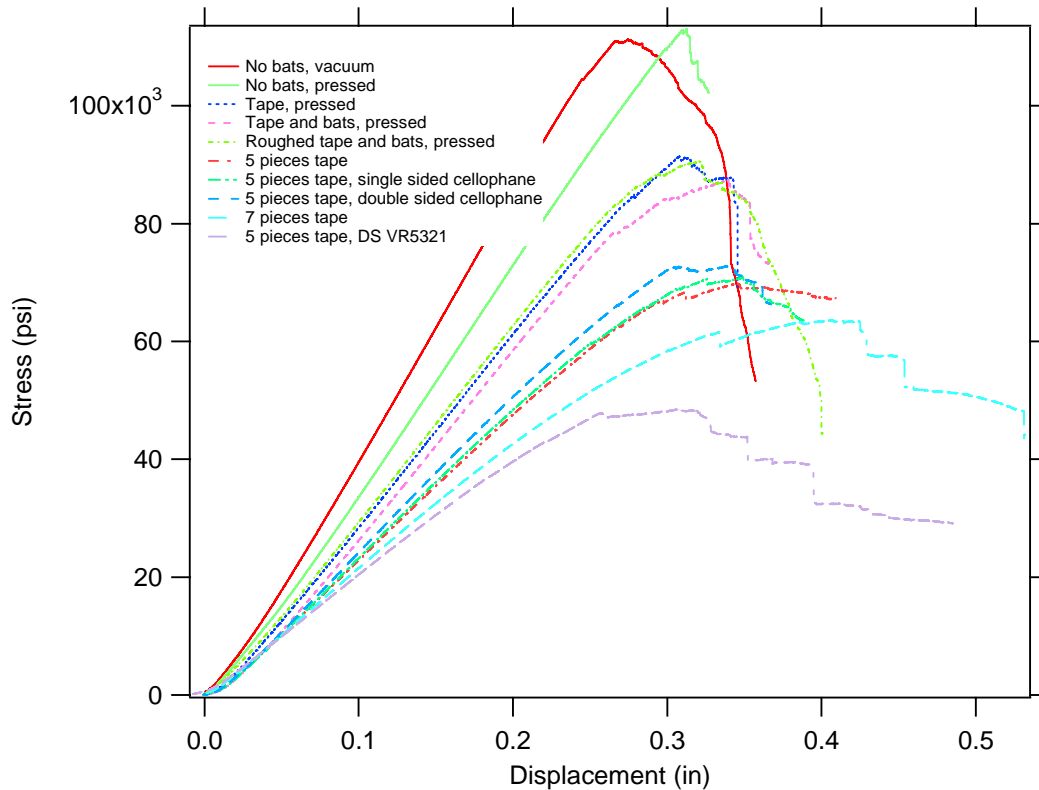


Figure 14. Maximum stress versus displacement in four-point-bend.

These experiments showed that the battery fibers degrade the structural response of the plate, probably because of the weak bond between the battery fibers and the surrounding matrix material. Different methods of preparing the encapsulating tape had little effect on structural behavior.

The four-point-bend test geometry produces a linear stress gradient through the thickness of the plate, with the maximum stress occurring at the plate surface. The battery fiber tows were placed just off the center of the plate cross section so they would experience minimum stress. As the load increased, the stress at the interface between the battery fiber tow and the matrix reached a critical point and failed. After this failure, the crack propagates through the rest of the plate, causing the entire plate to fail.

Finite element analyses provided insight into the interaction of the battery fiber tows with the other materials in the composite, indicating optimal battery locations within the composite structure. FEA also allows analysis of more complex structures. FEA results were used to enhance the design rules and tools and pointed to the need for new tests.

RULES AND TOOLS APPLICATION

Rules and tools that consider battery placement within the composite and the tradeoffs between power function and structural function are needed for power composite plate design. Power/energy and load-carrying capacity depend on the number of battery fiber tows and their placement. Typically, as the power/energy capacity is increased, the load-carrying capability of the composite is reduced, and vice versa. For a system-level design, compromises must be made between the optimal power configuration and the ultimate structural configuration. To find the best system-level design for power composite plates, the rules and tools must be implemented into a design program.

A web-based program was chosen as the platform for the rules and tools application because it allows simple interface design and runs on any computer with an internet connection and a web browser. The program has an easy-to-use interface that allows the designer to examine the tradeoffs between the power and structure functions of different plate designs.

We identified a challenge problem in the aircraft industry that can use our power composite technology. We collaborated with Boeing on developing a battery sandwiched between two piezoceramic plates that acts as a bender to harvest vibrational energy from an aircraft and can be used to power a remote sensor. We developed rules and tools specific to the design of such a battery and performed vibration tests on sample configurations.

We developed a simple rules and tools application for the design vibration-charged batteries. The vibration-charged batteries are bimorph benders constructed by sandwiching a power composite between two piezoceramic elements. The application takes user inputs, such as required battery power, component thicknesses, mechanical properties, and battery properties, and determines the optimal parameters for the bender.

The first step in the design process is to define the battery tow length based on the sensor power requirements. Next, restrictions on the overall length, thickness, and width of the bender were considered and dimensions and properties were calculated using the vibration characteristics of the base motion. The application then uses equations of motion to determine the natural frequencies and tip displacements for the bender. Once the overall dimensions are known, the composite battery configuration, including battery placement and fiber/matrix fractions, are determined.

Application Details

The application makes some assumptions and limitations in the design of the benders. The first is geometric constraints, as shown in Figure 15. The bender is constrained to be between 2.00-2.75 in. in length, and 0.20 to 0.50 in. in width. Due to the limited choices of piezoceramic elements, the thickness of the piezoceramic must be between 0.007 and 0.080 in. The power composite is constrained to be $0.9 \cdot t_p < t_b < 1.2 \cdot t_p$, where t_p is the piezoceramic thickness and t_b is the power composite thickness. These constraints limit the composite thickness to a minimum of 0.0063 and a maximum of 0.096 in.

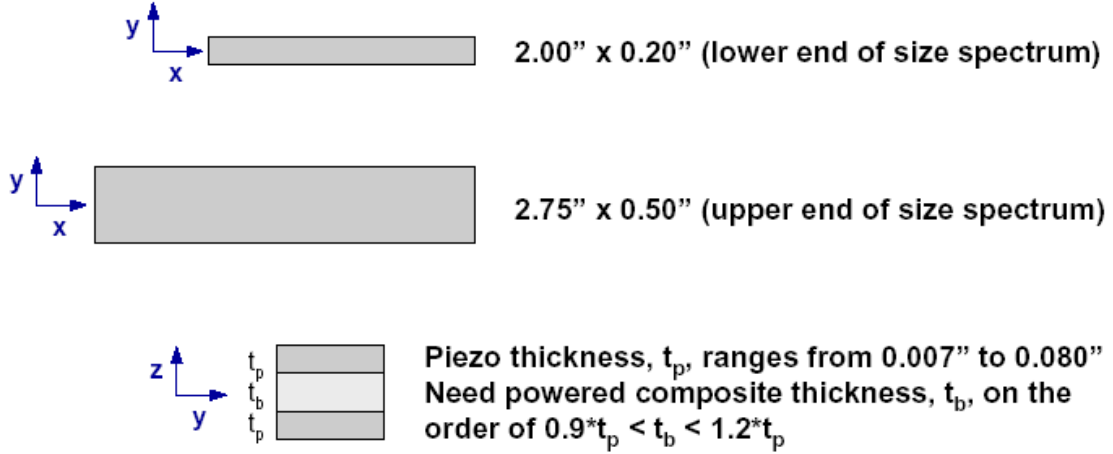


Figure 15. Bimorph size constraints.

The first step in designing the plates is to calculate the required length of battery tow based on the required power. The power composites considered here deliver low amounts of power; a typical value is 2.0 mW. The capacity per unit length of battery tow (an input value for the application) is typically about 2.0 A/mm. The battery voltage output (also an input for design) is typically about 3.0 V. The total length of power fibers necessary to deliver the required power is calculated using the standard power-voltage relationship given in Eqn 1:

$$l_{tow} = \frac{P_{req}}{V_{tow} I_{tow}} \quad \text{Eqn 1}$$

where l_{tow} is the minimum length of battery tow required, P_{req} is the power required, V_{tow} is the voltage per tow and I_{tow} is the battery tow capacity per length.

If the length of battery tow required is less than the minimum length for the bender, then the battery tow length is set to the length of the bender and a single tow is required. If the length of battery tow required exceeds the maximum bender length, then the battery is divided into multiple tows.

For a given first mode frequency of vibration, the other dimensions of the bimorph can be optimized once the minimum length of battery tow is known. The thicknesses of the available piezoceramic material are given as an input. A table of power composite thicknesses and lengths that will give a bender with the required frequency of vibration is then calculated. This calculation is based on constant cross section properties calculated using modulus-weighted values.

The first step in calculating the modulus-weighted properties is to determine the mass per unit length of the bender, using Eqns 2-4:

$$A_{layer} = t_{layer} W_{beam} \quad \text{Eqn 2}$$

$$M_{lpl} = A_{layer} \rho_{layer} \quad \text{Eqn 3}$$

$$M_{length} = \sum_{numLayers} M_{lpl} \quad \text{Eqn 4}$$

where t_{layer} is the thickness of a layer, W_{beam} is the width, and A_{layer} is the cross-sectional area for a given layer. M_{lpl} is the mass per unit length of a given layer, based on the density, ρ_{layer} , and area of the layer. The beam's mass per unit length, M_{length} , is then the sum of the mass per unit length of each layer.

Next, the bending moment of inertia for the beam is calculated by first transforming the layer widths using a reference modulus, as shown in Eqn 5:

$$w_t = \frac{E_i}{E_R} w_{beam} \quad \text{Eqn 5}$$

where w_t is the transformed layer width, E_i is the layer modulus, E_R is the reference modulus, and w_{beam} is the width of the beam (uniform width assumed for each layer).

The transformed area, A_{trans} is then calculated for each layer (Eqn 6). Using the transformed areas, the centroid, \bar{y} , and moment of inertia, I_0 , about the centroidal axis is computed (Eqns 7-8). Finally, the bending moment of inertia, I , is found for the beam cross section (Eqn 9).

$$A_{trans} = w_t t_{layer} \quad \text{Eqn 6}$$

$$\bar{y} = \frac{\sum A_{trans} y_{layer}}{\sum A_{trans}} \quad \text{Eqn 7}$$

$$I_0 = w_{trans} t_{layer}^3 \quad \text{Eqn 8}$$

$$I = \sum \left(I_0 + A_{trans} (y_{layer} - \bar{y})^2 \right) \quad \text{Eqn 9}$$

Once the beam's bending moment of inertia and mass are calculated, the first five fundamental frequencies are calculated using the standard formula for a vibrating beam (Eqn 10):

$$f_i = \frac{\lambda^2}{2\pi l_{beam}^2} \sqrt{\frac{E_R I}{m}} \quad \text{Eqn 10}$$

where f_i is the frequency for mode i and λ takes on the values 1.875, 4.694, 7.855, 10.996, and 14.137 for the first through fifth frequencies, respectively.

Next, the range of beam thicknesses and lengths that give the desired natural frequency are chosen. Any of these beams would produce the desired response, but in the interest of minimizing weight and size, the beam with the smallest length and thickness is selected for the design.

Once the beam dimensions are known, the motion of the beam can be calculated and subsequently the power output by the piezoceramic can be calculated. The motion of the beam is calculated by solving the equation of motion for a vibrating beam, as described in Clough and Penzien³. First, the base motion, v_g , is assumed to be sinusoidal at the given input frequency, f , and amplitude, a (Eqn 11). A shape function, ψ , is assumed to fit the first mode of vibration and is dependent on the distance, x , along the beam and the beam length, l (Eqn 12). The generalized mass, m^* , and stiffness, k^* , are calculated using the shape function, the mass distribution along the beam, m , the Young's modulus, E , and the beam bending moment of inertia, I . For these calculations, E is the reference modulus and I is that calculated from Eqn 9. The undamped natural frequency, ω , for this mode of vibration is found using the generalized mass and stiffness. The equation of motion for the vibrating beam is then solved using the Duhamel approach, and the vibration integral (Eqn 16) is solved. From the integration of Eqn 16 and the generalized coordinates of Eqn 17, the motion of the beam, v , and the tip, v_{tip} , is found (Eqns 18-19):

$$v_g(t) = a \sin ft \quad \text{Eqn 11}$$

$$\psi(x) = 1 - \cos \frac{\pi x}{2l} \quad \text{Eqn 12}$$

$$m^* = \int_0^l m(x) \psi(x)^2 dx \quad \text{Eqn 13}$$

$$k^* = \int_0^l EI \psi(x)^2 dx \quad \text{Eqn 14}$$

$$\omega = \sqrt{\frac{k^*}{m^*}} \quad \text{Eqn 15}$$

$$V(t) = \int_0^t v_g''(\tau) e^{-\xi\omega(t-\tau)} \sin \omega(t-\tau) d\tau \quad \text{Eqn 16}$$

$$Z(t) = V(t) \frac{\int_0^l m(x) \psi(x) dx}{m^* \omega} \quad \text{Eqn 17}$$

³ R. W. Clough and J. Penzien, *Dynamics of Structures*, McGraw Hill, 1975

$$v(x, t) = Z(t)\psi(x) \quad \text{Eqn 18}$$

$$v_{tip}(x, t) = v_g(t) + v(x, t) \quad \text{Eqn 19}$$

This methodology is implemented in a series of web-based applications.

Web Applications

The first tool of the web-based application, the Natural Frequency Calculator (NFC), is shown in Figure 16. The user enters dimensions and material properties for two bender designs, and the NFC calculates the first five natural frequencies. This tool allows a designer to see the effects of different design parameters on the natural frequencies of the bender.

Figure 16. Natural Frequency Calculator.

Table 3 shows an example comparing two benders with difference materials in the middle layer. Design A uses properties for three layers of piezoceramic, and Design B uses a middle layer of composite material between two piezoceramic layers. As shown in the table, the higher modulus and lower density of the composite layer for Design B increase the first natural frequency by nearly 19%.

Table 3. Sample data from the Natural Frequency Calculator.

Parameter	Design A	Design B
Beam Width (mm)	10.0	10.0
Beam Length (mm)	58.0	58.0
Layer 1 Thickness (mm)	2.0	2.0
Layer 2 Thickness (mm)	2.3	2.3
Layer 3 Thickness (mm)	2.0	2.0
Layer 1 Young's Modulus (GPa)	66	66
Layer 2 Young's Modulus (GPa)	66	84
Layer 3 Young's Modulus (GPa)	66	66
Layer 1 Density (kg/m ³)	7800	7800
Layer 2 Density (kg/m ³)	7800	1800
Layer 3 Density (kg/m ³)	7800	7800
Reference Modulus (GPa)	66.0	66.0
Beam Inertia (m ⁴)	2.08E-10	2.11E-10
First Natural Frequency (Hz)	880	1045
Second Natural Frequency (Hz)	5515	6546
Third Natural Frequency (Hz)	15443	18331
Fourth Natural Frequency (Hz)	30262	35922
Fifth Natural Frequency (Hz)	50021	59375

The second tool calculates the bending response of two benders to a given input frequency and amplitude, as shown in Figure 17. This application allows the user to see the response effects of varying plate dimensions, damping, and input motion parameters. Design B in Table 3 was run using this application to determine the difference in tip motion for 5% and 40% damping. The clamped end of the beam was excited with an input frequency of 1000 Hz and an amplitude of 0.0127 mm (Figure 18). The beam with less damping shows an overshoot in the tip response, but eventually settles to a steady-state amplitude of 0.9 mm (Figure 19). The beam with more damping does not show the strong transient response of the other beam, and quickly reaches a steady state response of 0.02 mm.

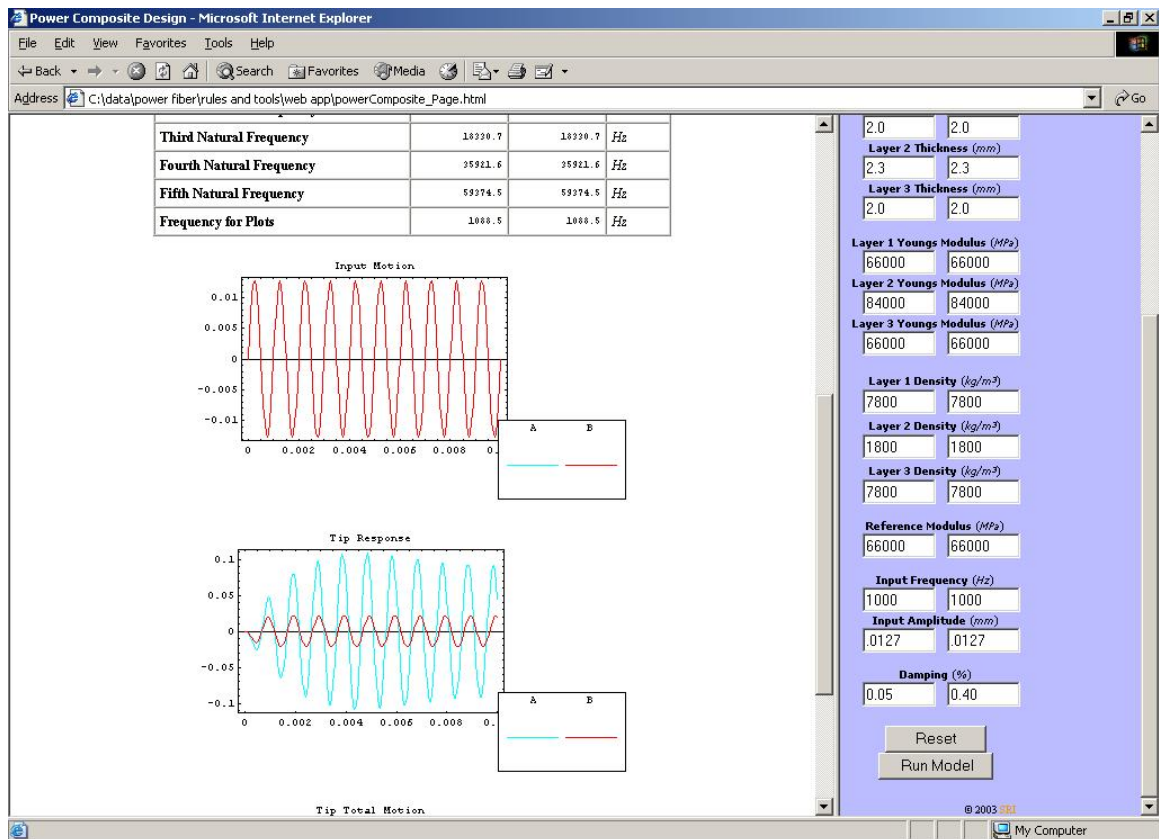


Figure 17. Screen shot of bending response tool.

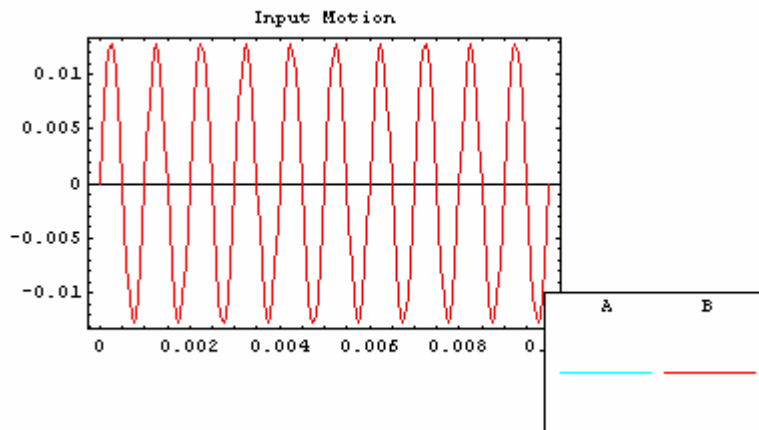


Figure 18. Input motion for vibration with 5% damping (A) and 40% damping (B).

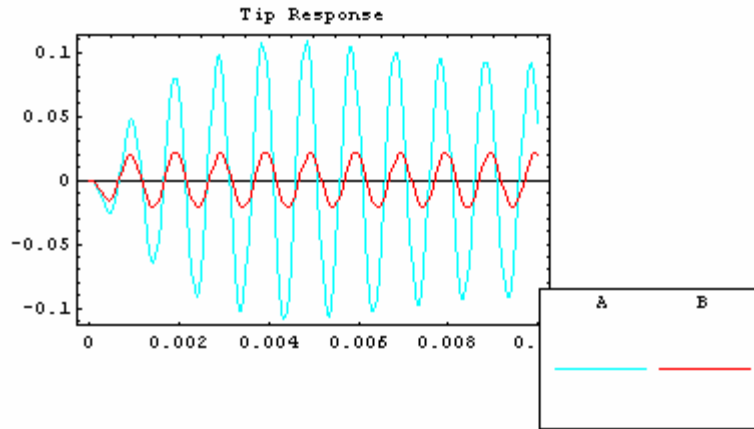


Figure 19. Tip response with 5% damping (A) and 40% damping (B).

The third tool computes the required size of the bender components for resonant vibration at a given frequency. The user inputs the amount of power required from the battery, the input frequency and amplitude, and some parameters regarding the piezoceramic thickness and battery characteristics. The final design is then computed using the procedure outlined above.

Figure 20 shows screen shots from a run requiring 2.0 mW of power, with an input frequency of 1000 Hz and an amplitude of 0.0127 mm. The battery is assumed to have a capacity of 2.0 A/mm and an output voltage of 3.0 V. The piezoceramic plates for this design are 2.2 mm thick, and a standard carbon/epoxy composite is assumed for the composite battery. For typical designs, only a single battery tow is required. Figure 21 shows the beam length and power composite thickness combinations that will give a bimorph with the required natural frequency. The minimum length for the beam is 56.5 mm, and the minimum thickness required for the composite battery is 1.8 mm, thus defining the final size of the vibration-charged battery. We have shown in testing that a similar sized bimorph will generate sufficient voltage to power the battery if the proper conditioning electronics are applied.

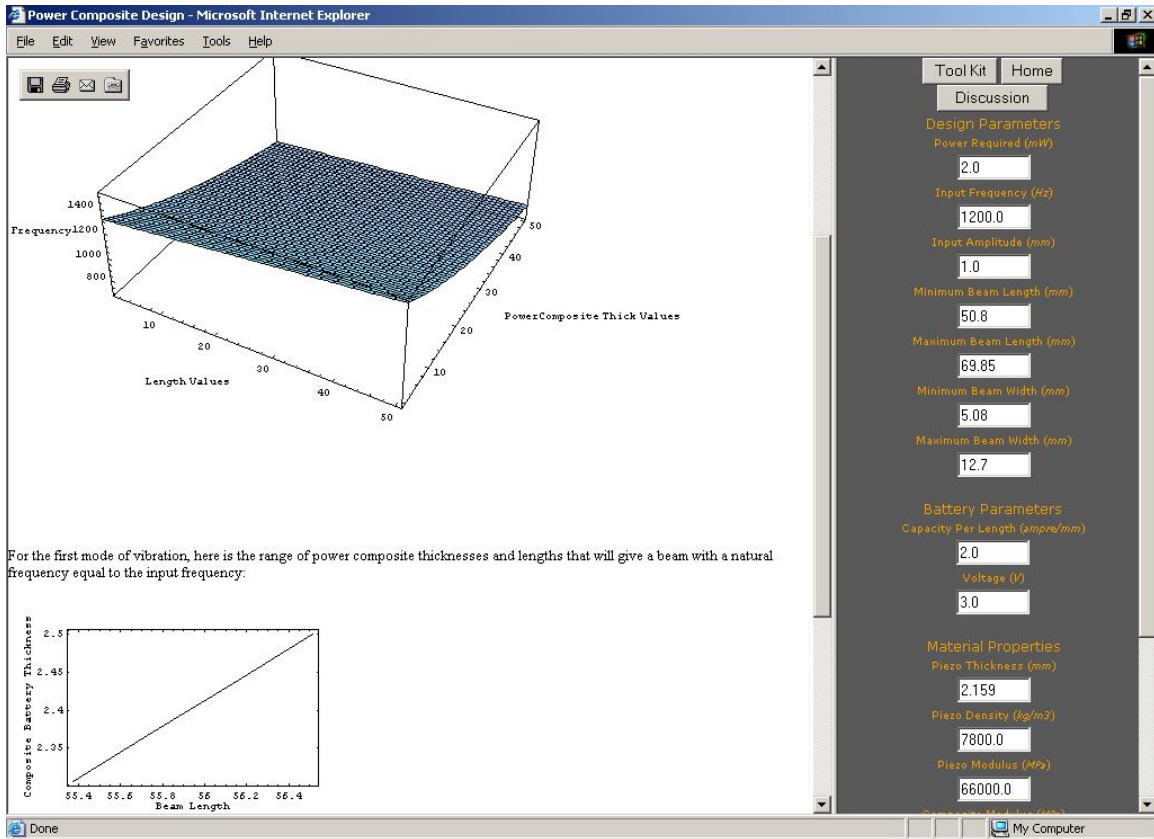


Figure 20. Vibration-charged battery design tool.

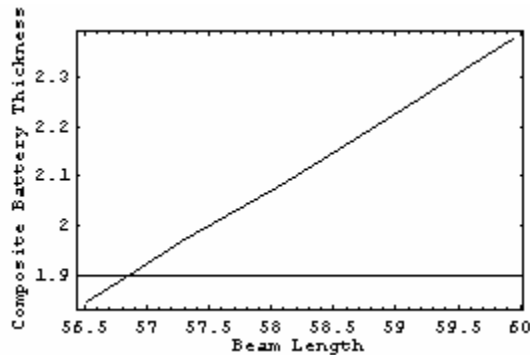


Figure 21. Range of composite thicknesses and beam lengths that yield the desired resonant frequency.

Future Work

Based on initial test data, the current equations of motion do an adequate job of predicting the motion of the bender. Additionally, the power generated by the bender in testing appears to be enough to charge the battery. To be more precise, and to calculate the power generated by the bimorph, the piezoceramic constitutive equations should be solved with the bimorph equation of motion.

The constitutive relationship of the bimorph is such that the stress and power output are closely coupled. The piezoceramic constitutive relationships are shown in stress/charge form in Eqn 20:

$$\begin{Bmatrix} T_{11} \\ D_3 \end{Bmatrix} = \begin{bmatrix} c^E & -e^t \\ e & \epsilon^S \end{bmatrix} \begin{Bmatrix} S_{11} \\ E_3 \end{Bmatrix} \quad \text{Eqn 20}$$

where T_{11} is the stress (N/m^2), S_{11} is the strain (m/m), D_3 is the charge density (C/m^2), E_3 is the electric field (N/C), c^E is a stiffness coefficient (N/m^2) with no electrical field, e^t (superscript t is for the matrix transpose) and e are piezoelectric coupling coefficients (N/m^2), ϵ^S is the electric permittivity (F/m) with no strain field. This constitutive relation would then be solved with the beam equation of motion and the piezo charge equation,

$$\begin{bmatrix} m & 0 \\ 0 & 0 \end{bmatrix} \begin{Bmatrix} \ddot{d} \\ \ddot{V} \end{Bmatrix} + \begin{bmatrix} k^E & -p^t \\ p & C^S \end{bmatrix} \begin{Bmatrix} d \\ V \end{Bmatrix} = \begin{Bmatrix} -m_f a_{in} \\ Q \end{Bmatrix} \quad \text{Eqn 21}$$

where m is the mass, d is the displacement, k^E is the stiffness, p is a piezoelectric coupling coefficient, a_{in} is the input acceleration, V is the piezo voltage, C is related to the electric permittivity, and Q is the electric charge.

Solving this system of equations would give both the beam motion and the voltage produced by the piezoceramic. From the piezoceramic voltage produced, the power output can be calculated, and the conditioning electronics for charging the battery computed.

FINITE ELEMENT CALCULATIONS

Approach

We used the finite element method (FEM) to confirm the accuracy of the simple resonant frequency model, and to determine the material properties that have the largest effect on the bending first mode vibration. We calculated the first three bending mode resonant frequencies using LS-DYNA3D (www.lstc.com) on a Linux cluster.

We first compared the resonant bending frequencies for a single piezo electric beam. The beam was 0.08 inches thick, 2.3 in. long, and 0.40 in. wide. We tested this beam in our vibration test facility and found the first natural frequency to be 292 Hz. This value compares well with the simple model, 279 Hz, and the FEM using an isotropic material model, 265 Hz. These differences in this first resonant frequency may be attributed to differences in the test and model boundary conditions, beam/vibrator interaction in the tests, and differences in the published Young's modulus versus the actual value.

We then looked at the effects of different material parameters on the resonant bending frequencies for a carbon/epoxy beam. The first three bending natural frequencies were calculated using an orthotropic material model, while different parameters were varied. The two most significant parameters, Young's modulus in the axial direction and the shear modulus, had the greatest effect on the bending frequencies, as shown in Table 4. It was found that lowering

the Young's modulus by two orders of magnitude along the beam axis reduced the first bending natural frequency by 75%. Similarly, lowering the shear modulus by two orders of magnitude resulted in an 81% reduction in the first bending natural frequency. The axial Young's modulus and the shear modulus were the only material properties found to have a pronounced effect on the bending natural frequencies, and only when changed by orders of magnitude from the baseline.

Table 4. Effect of shear modulus, G, and axial Young's modulus, E, on natural frequencies in bending.

Property	Baseline	Low G	Young's Modulus
E _a (psi)	7.18E+05	7.18E+05	7.18E+05
E _b (psi)	1.22E+07	1.22E+07	7.18E+05
E _c (psi)	7.18E+05	7.18E+05	7.18E+05
V _{ba}	0.28	0.28	0.28
V _{ca}	0.28	0.28	0.28
V _{cb}	0.02	0.02	0.28
G _{ab} (psi)	2.80E+05	2.80E+02	2.80E+05
G _{bc} (psi)	2.80E+05	2.80E+02	2.80E+05
G _{ca} (psi)	2.80E+05	2.80E+02	2.80E+05
First freq. (Hz)	691	133	172
Second freq. (Hz)	4028	400	1068
Third freq. (Hz)	10243	680	2966

We expanded the design model for fiber batteries to include the more complex geometry of the PZT tubes; demonstrated the function of the fiber battery power composite; and validated the updated model with a fabricated fiber-composite cantilever beam. The model is used to estimate the structural response and power output of a specified composite design to a given ambient vibration spectrum. The same fundamental principles for calculating bending moment of inertia and fundamental frequencies were used for this analysis. However, we used a closed-form solution to calculate the tip motion of a damped oscillating system [2]. This motion may be solved using the separation of variables method:

$$v(x, t) = v(t)\Psi(x) . \quad \text{Eqn 22}$$

The time-dependent equation of motion for a cantilevered beam is

$$\ddot{v} + 2\xi\omega\dot{v}(t) + \omega^2 v(t) = a \sin \omega t \quad \text{Eqn 23}$$

and the assumed shape function for this design is

$$\Psi(x) = 1 - \cos \frac{\pi x}{2L} , \quad \text{Eqn 24}$$

where ξ is the damping ratio, ω is the harmonic loading frequency, L is the length of the beam, and x is the distance from the base of the beam. The general solution to Eqn 4 is

$$v(t) = v_h(t) + v_p(t) \quad \text{Eqn 25}$$

and the homogeneous solution is

$$v_h(t) = e^{-\xi \hat{\omega} t} (A \sin \hat{\omega}_D t + B \cos \hat{\omega}_D t) , \quad \text{Eqn 26}$$

where

$$A = -\left(\frac{a}{\hat{\omega}_D} \right) \left[\frac{\omega(1 - \beta^2) + 2\hat{\omega}\xi^2\beta}{(1 - \beta^2) + (2\xi\beta)^2} \right] \quad \text{Eqn 27}$$

$$B = \frac{-2a\xi\beta}{(1 - \beta^2)^2 + (2\xi\beta)^2} \quad \text{Eqn 28}$$

Here, $\hat{\omega}$ is the first fundamental frequency of the beam, β is the ratio of the harmonic loading frequency to the first fundamental frequency ($\omega/\hat{\omega}$), and the first fundamental damped frequency may be calculated as

$$\hat{\omega}_D = \hat{\omega} \sqrt{1 - \xi^2} . \quad \text{Eqn 29}$$

The particular solution is

$$v_p(t) = G_1 \sin \omega t + G_2 \cos \omega t , \quad \text{Eqn 30}$$

where

$$G_1 = \frac{a(1 - \beta^2)}{(1 - \beta^2)^2 + (2\xi\beta)^2} \quad \text{Eqn 31}$$

$$G_2 = \frac{-2a\xi\beta}{(1 - \beta^2)^2 + (2\xi\beta)^2} . \quad \text{Eqn 32}$$

The relative displacement at the tip of the vibrating beam may be calculated with respect to the base displacement as

$$v_{tip}(t) = v(L, t) + a \sin \omega t . \quad \text{Eqn 33}$$

Because the voltage produced across the piezo thickness is a direct function of the material strains, the strain across the beam length must be calculated:

$$\varepsilon(x, t) = \frac{M(x, t)y}{EI} \quad \text{Eqn 34}$$

where

$$M(x, t) = v(t) \cdot \frac{d^2 \Psi(x)}{dx^2} = v(t) \cdot \frac{d^2 \left[1 - \cos\left(\frac{\pi x}{2L}\right) \right]}{dx^2} \quad \text{Eqn 35}$$

The resulting strain distribution along the length of the beam for the assumed shape function Ψ is

$$\varepsilon(x, t) = \frac{\pi^2 y}{4EIL^2} v(x, t) \quad \text{Eqn 36}$$

and the averaged time-dependent strain along the beam is

$$\varepsilon_1^* = \varepsilon(x, t) \cdot \varepsilon_f \quad \text{Eqn 37}$$

where ε_f is the shape function-dependent strain averaging factor. The strain averaging factor for the assumed shape function Ψ is 0.365. Eqn 33 is then substituted into Eqn 16 to calculate the voltage output for the given beam design under a user-defined vibration environment.

This model was implemented in MATLAB to evaluate the mechanical response and resulting strain-based voltage output for a range of flat-plate and PZT tube bender designs.

MODEL CALIBRATION

Bender Design: PZT/Aluminum Sandwich Beam

We used a simple PZT/aluminum sandwich beam design to calibrate the analytic model. This three-layer beam design uses commercially available products with known material, mechanical, and electrical properties (Table 5 and Table 6). The ultimate tensile stress and strain-to-failure of the PZT material are 76 MPa and 0.15%, respectively. A silver-impregnated epoxy resin bonds one upper and one lower nickel-plated, 1.016-mm-thick PZT plate to a single 1.315-mm-thick aluminum spacer. The epoxy serves as both a mechanical bonding agent and a conducting element between the nickel electrodes on the inner surfaces of the two PZT plates. We measured the capacitance of each PZT plate to be 10.4 nF, which is very close to the calculated capacitance of 9.98 nF using Eqn 1. The stacked configuration and dimensions for this beam design are shown in Figure 22 and Figure 23.

Table 5. Piezoceramic properties for 1.016-mm-thick PZT A4 plates.

Property		Value
Piezoelectric Charge Coefficient, d_{31}		$190 \text{ m/V} \times 10^{-12}$
Piezoelectric Voltage Constant, g_{31}		$-11.6 \text{ Vm/N} \times 10^{-3}$
Capacitance, C_p	Calculated	10.4 nF
	Measured	9.98 nF

Table 6. Material properties for PZT A4 and aluminum.

Property	Aluminum	PZT A4
Density, ρ	2.70 g/cm^3	7.80 g/cm^3
Young's Modulus, E	70 GPa	66 GPa

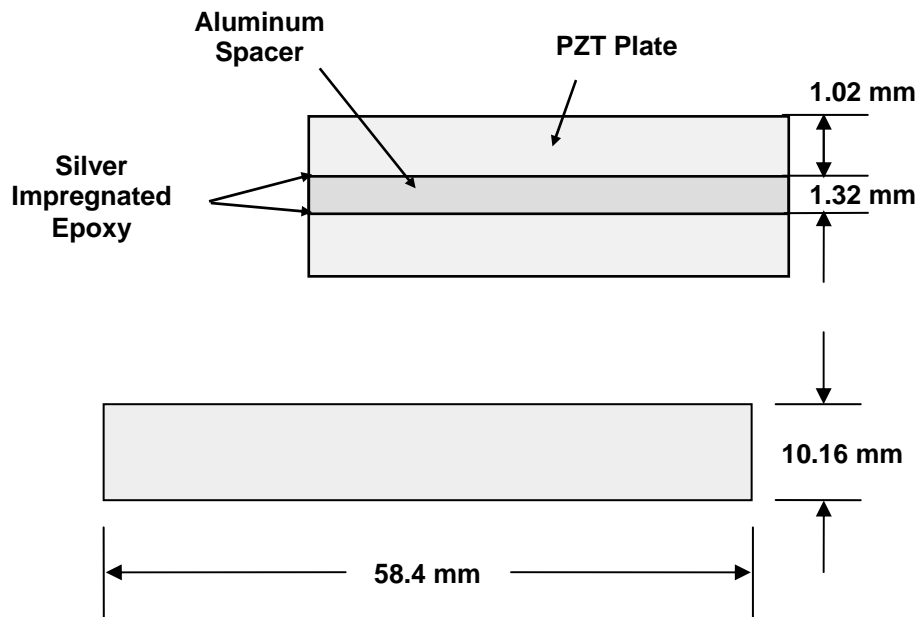


Figure 22. Cross-sectional and top view schematics of the 3-layer PZT/Aluminum sandwich beam (not to scale).

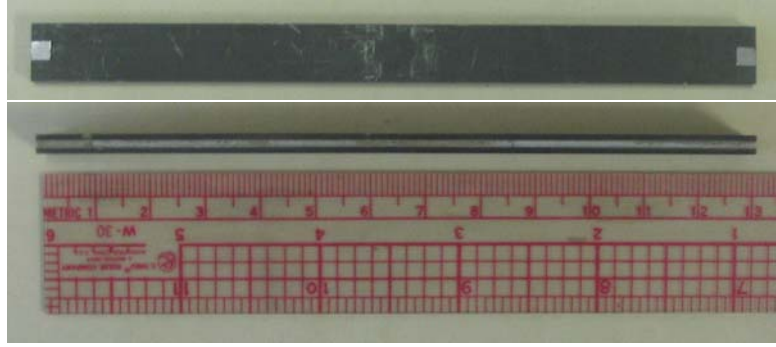


Figure 23. Photo of the 3-layer PZT/aluminum sandwich beam.

Experimental Setup

We modified a previously built test rig [1] to characterize the harmonic response and voltage output of the three-layer sandwich beam (Figure 23). The test rig houses the mechanical shaker (LDS V203, Test Measurements Ltd., Royston, England) and isolates the measurement system from the operating vibrations during testing. A sinusoidal signal generator and 50-A amplifier power the input frequency and amplitude signal for the vibrating head of the shaker. Three fiber optic sensors (MTI 2000 Fotonic Sensor, MTI Instruments, Latham, NY) are used to measure displacements of the shaker head and each of the two beam tips, as shown in Figure 24. We used a digital oscilloscope (Nicolet 490, Test Measurements Ltd., Royston, England) to record base displacement, tip displacements, and PZT output voltage.

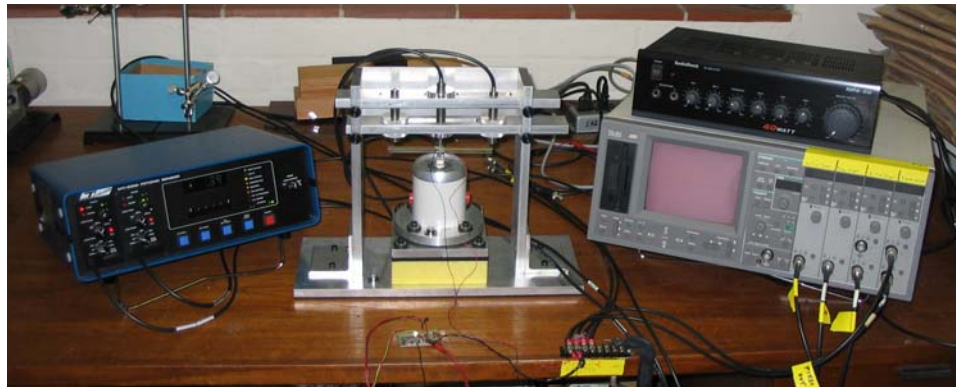


Figure 24. Photograph of the experimental setup.

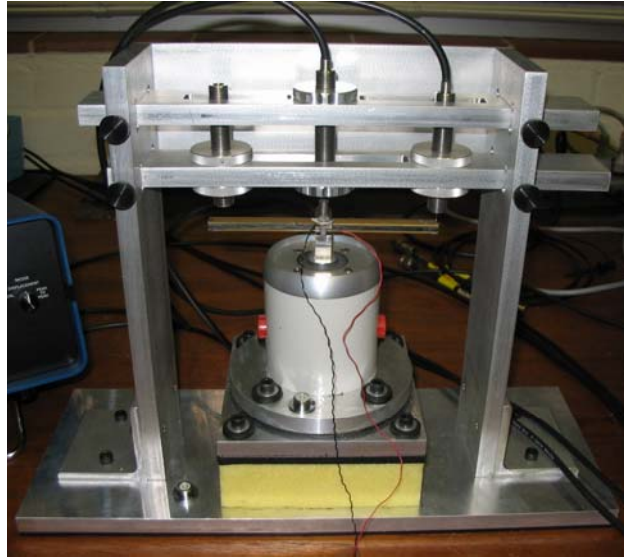


Figure 25. Photograph of the vibration test rig.

Bender Performance

The natural frequencies and damping coefficient depend on the design and fabrication of a bending element. We measured the first harmonic frequency and damping coefficient of the three-layer PZT beam by first securing the shaker head to resist axial and lateral motion, providing an impulsive point load to the tip of the beam, and then recording the tip displacement during the free vibration response (Table 7). From the free vibration response in Figure 26, we can measure the fundamental frequency of vibration and the structural damping coefficient as a percentage of critical damping [R.W. Clough and J. Penzien, “Dynamics of Structures,” McGraw-Hill Inc., 1975].

Table 7. Vibration Response of PZT 3-layer beam.

First Harmonic Frequency (Hz)	Damping Coefficient
456 Hz	1.6 %

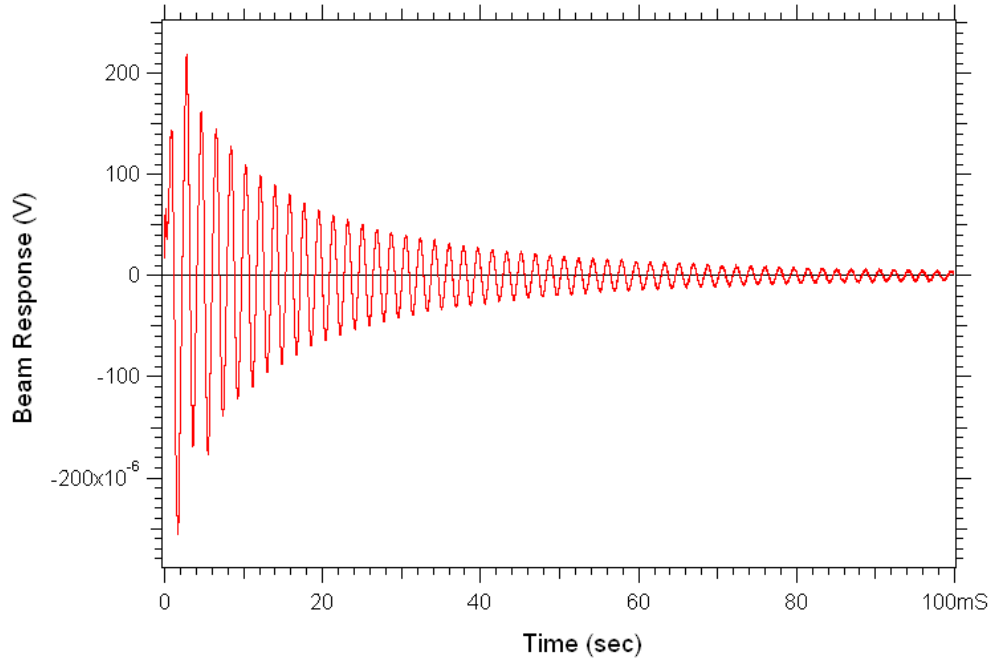


Figure 26. Free vibration response of the PZT/aluminum sandwich beam.

When the shaker head is driven by a constant sinusoidal frequency, the beam tip responds with a displacement at the same frequency. The strains that develop in the bending piezo plates produce an output voltage that is proportional to the relative tip displacement. The plot in Figure 27 shows the relative tip and voltage output response to a $\pm 2\text{-}\mu\text{m}$ base displacement when driven at 525 Hz.

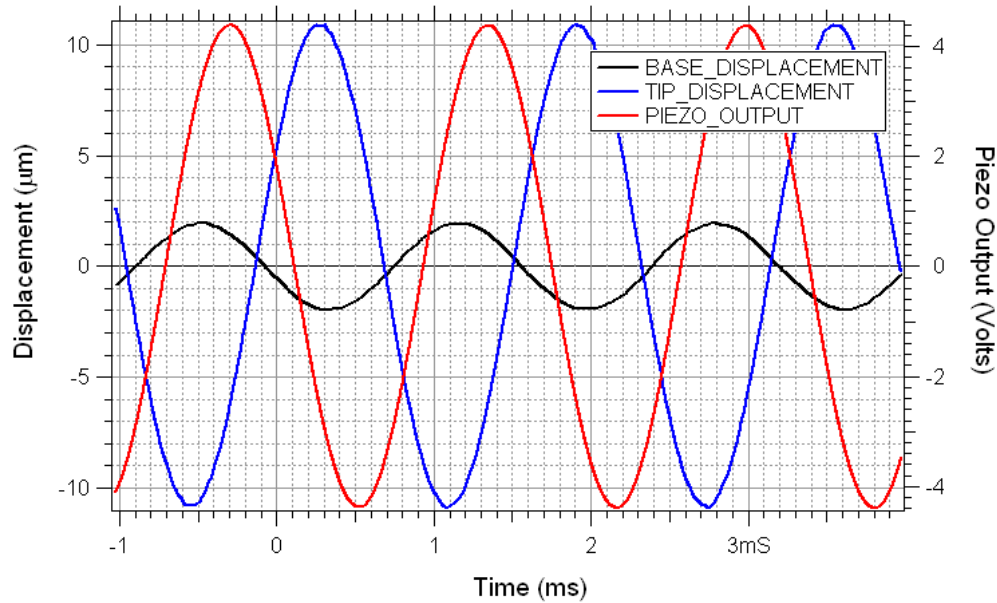


Figure 27. Tip displacement and piezo voltage output for a given sinusoidal base displacement of the PZT/aluminum sandwich beam at 525 Hz.

Model Performance

To test the performance of the analytic model, we measured and recorded tip displacement with a constant 1- μm base displacement over a range of frequencies surrounding the first natural frequency of the beam. We used the results of the three-layer bender tests to calibrate our analytic model. With a damping ratio of 1.6%, the tested tip displacement matches the model output well for frequencies on either side of the resonant frequency of the beam (Figure 28). However, the model overpredicts the tip displacement in the range 505 ± 10 Hz. This overprediction may result from a combination of two factors. First, the model does not consider the mechanical contribution of the silver-impregnated epoxy in the vibrational response of the beam. Second, the peak tip displacement is extremely sensitive to changes in frequency near resonance, and it is possible that we did not capture the true resonating tip response. Finally, the damping coefficient is greatest at high amplitude during free vibration, and decreases as the amplitude decays over time. This indicates that the damping ratio is a function of vertical beam tip acceleration and varies with driving frequency and amplitude. In fact, a ten percent adjustment of the damping ratio in the design model results in a ten percent reduction in voltage output.

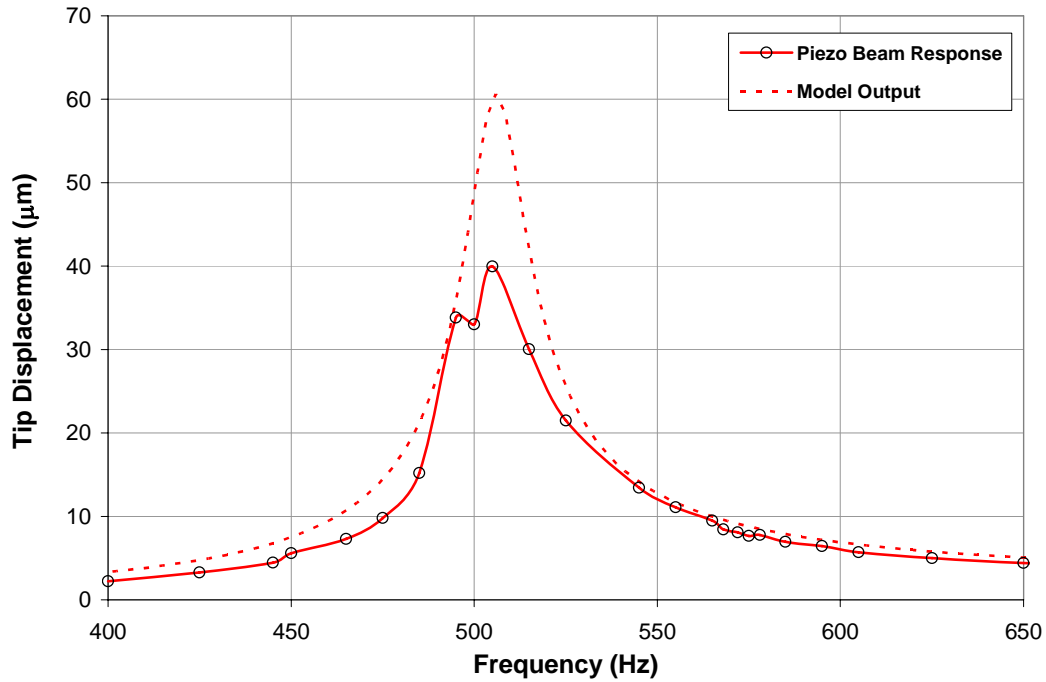


Figure 28. Measured and calculated tip displacement for the PZT/aluminum sandwich beam.

The model predicts output voltage within 10% of the measured voltage at 505 Hz, as shown in Figure 29. The irregular output voltage for frequencies greater than 505 Hz results from the structural coupling between the beam and shaker. This coupling may be characterized as the superposition of two spring-mass systems.

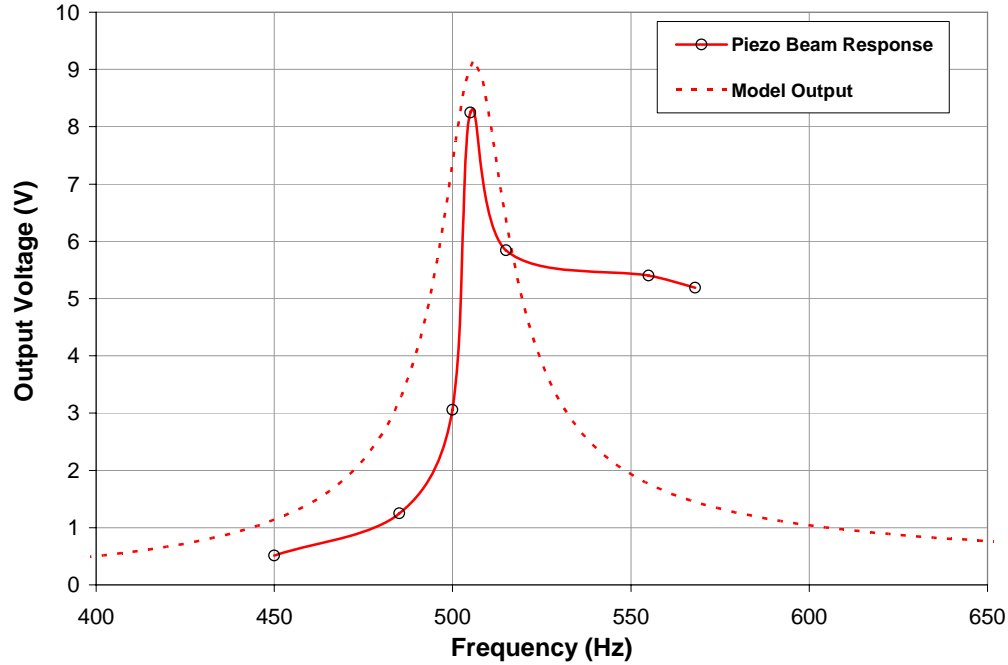


Figure 29. Measured and calculated voltage output for the PZT/aluminum sandwich beam.

MODEL DEMONSTRATION AND VALIDATION

Bender Design: Carbon Composite/PZT Tube Beam

To validate the analytical model, we used a three-layer carbon fiber composite/power fiber sandwich beam design with outside dimensions similar to those of the calibration beam. This three-layer beam design required several custom components with known and measured material, mechanical, and electrical properties (Table 8 and Table 9). We embedded one fully electroded and poled PZT tube and 13 unplated PZT tubes in a 1.60-mm-thick epoxy resin matrix (EPON 862), as shown in the schematic and photograph in Figure 30 and Figure 31. One each of these PZT-matrix layers was bonded to the upper and lower surfaces, respectively, of a 2.50-mm-thick carbon fiber plate. The complete carbon composite/PZT tube beam was 11 mm wide, 67.05 mm long and 5.7 mm wide. We measured the capacitance of the PZT tubes to be 13.4 ± 2.3 nF, which bounds the calculated capacitance of 11.9 nF as calculated using Eqn 1.

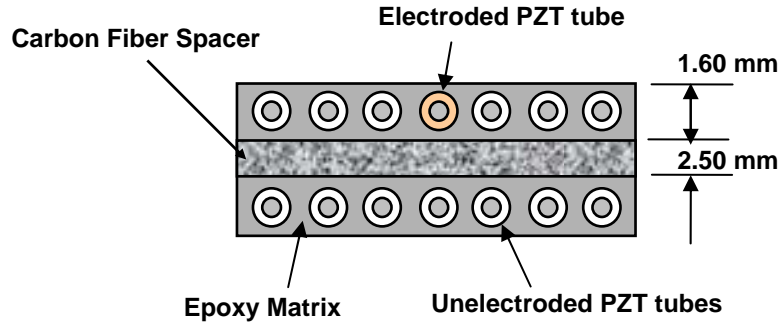


Figure 30. Schematic of carbon fiber/PZT tube/epoxy matrix sandwich beam.

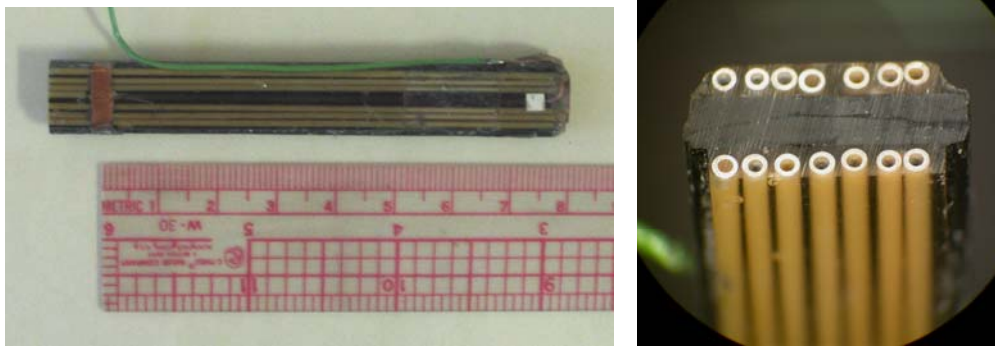


Figure 31. Photos of fabricated carbon fiber/PZT/epoxy matrix sandwich beam.

Table 8. Piezoceramic properties for 1.15-mm-OD, 0.65-mm-ID PZT 5A1 tubes.

Property		Value
Piezoelectric Charge Coefficient, d_{31}		$185 \text{ m/V} \times 10^{-12}$
Piezoelectric Voltage Constant, g_{31}		$25.5 \text{ Vm/N} \times 10^{-3}$
Capacitance, C_p	Calculated	11.9 nF
	Measured	$13.4 \pm 2.3 \text{ nF}$

Table 9. Material properties for carbon fiber plate, epoxy matrix and PZT 5A1.

Property	Carbon Fiber	Epoxy Matrix	PZT 5A1
Density, ρ	1.80 g/cm ³	1.20 g/cm ³	7.80 g/cm ³
Young's Modulus, E	84 GPa	2.6 GPa	66 GPa

Bender Performance

The first harmonic frequency and damping coefficient were measured using the same technique used for the piezo plate three-layer beam (Table 10).

Table 10. Vibration response of the carbon fiber/PZT/epoxy matrix sandwich beam.

First Harmonic Frequency (Hz)	Damping Coefficient
585 Hz	1.5 %

We performed a frequency sweep over the range 450-700 Hz with an input amplitude of 1.95 μm . The tip displacement and voltage results from these tests are plotted in Figure 32.

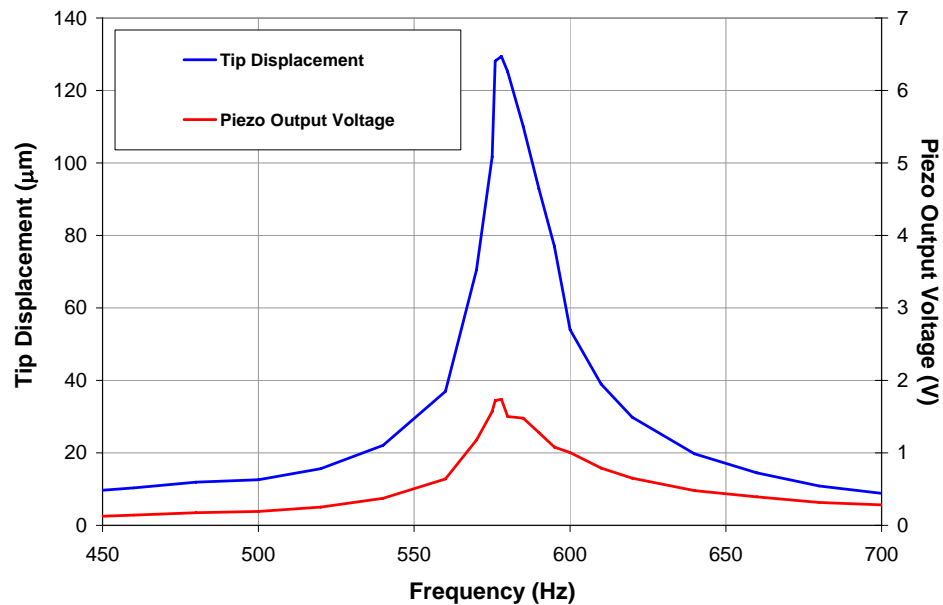


Figure 32. Measured tip displacement and output voltage for the PZT tube beam.

Model Performance

The data collected from the carbon fiber/PZT bender frequency sweep were used to validate our calibrated analytic harmonic and piezo response model. As shown in Figure 33, the measured tip displacement and piezo voltage output closely match the model predictions for a composite bender with a single electroded PZT tube driven with a 1.95- μm base displacement over the tested frequency sweep. This indicates that the shape function-based strain averaging factor, ε_f , that was used for the PZT plate three-layer bender also applies to the carbon fiber/PZT tube bender.

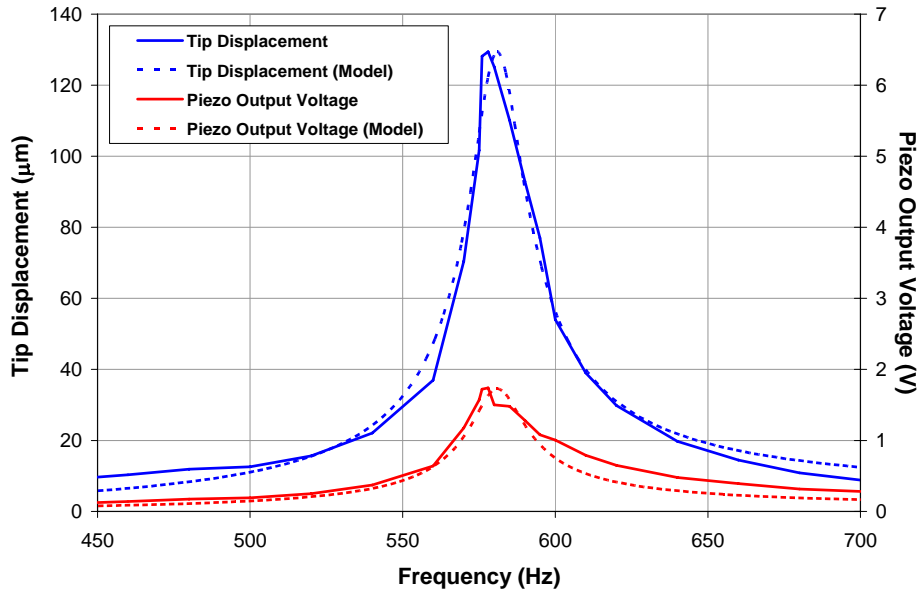


Figure 33. Measured and calculated tip displacement and output voltage for the PZT tube beam.

BENDER-BATTERY INTERACTION

When electrically coupled, the output produced by the PZT bender must be compatible with the charge limitations of the enclosed fiber battery. The maximum charging current for the fiber battery is 50 μA . To match this charging current through the signal conditioning circuit, we reduced the base amplitude and measured output voltage for a load resistance range of 2 k Ω -550 k Ω . Figure 34 shows a plot of output voltage, output current, and power generated by the bender over the tested range of resistances. At a charging current of 50 μA , the output voltage and power generated by this bender are approximately 0.64 V and 1.28 mW, respectively. This plot may be used to determine the number of electroded and poled PZT fibers required to charge at the full voltage capacity of the battery. For example, six poled tubes placed in series would produce 3.84 V at 50 μA . Thus, the battery and bender characteristics may be adjusted to adapt to the specific requirements of each application. Figure 35 shows the voltage-time charge history for the bender-battery system and the discharge characteristics when the system is discharged through a single LED.

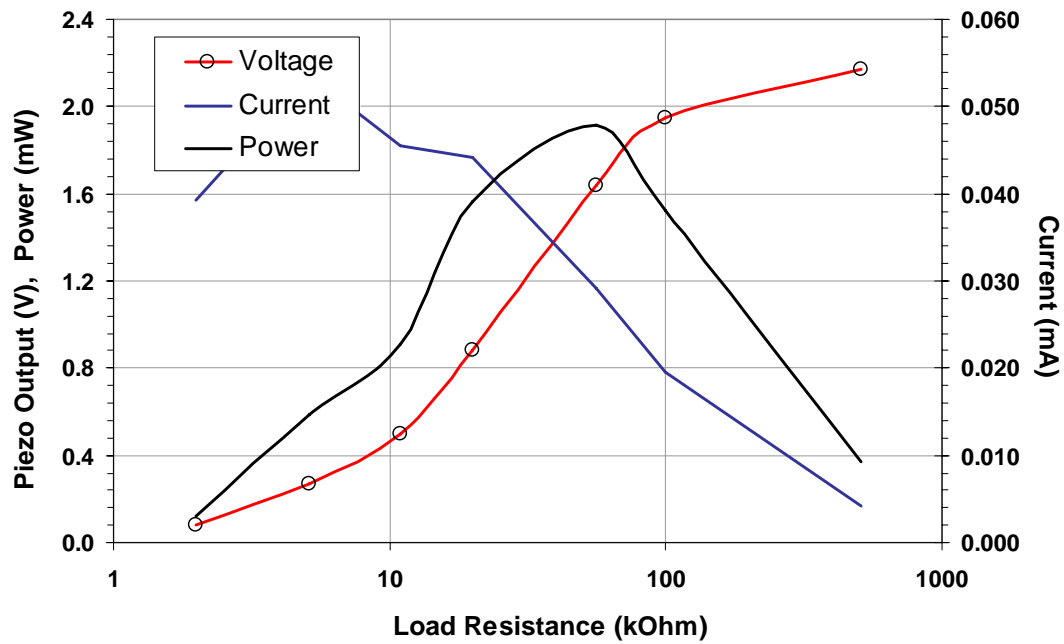


Figure 34. Voltage, current, and power output for the PZT tube beam.

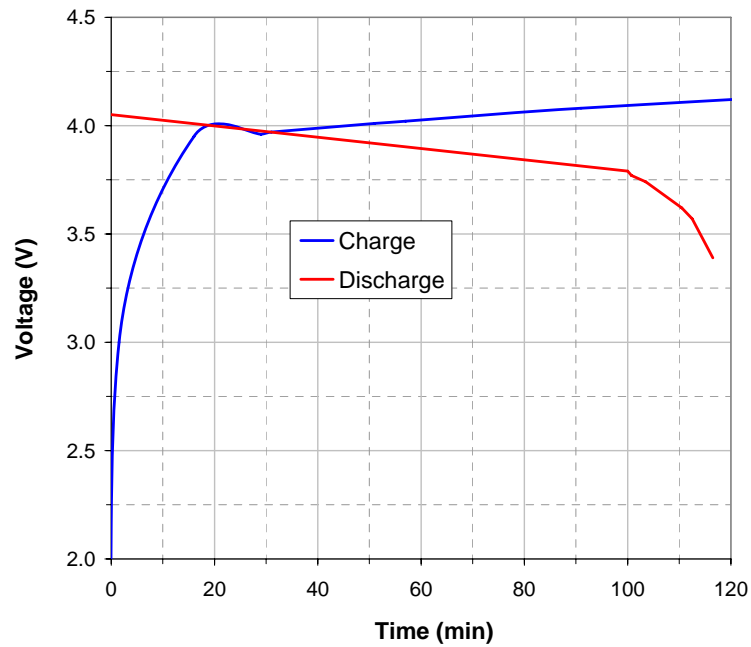


Figure 35. Lithium-ion battery charge and discharge curves.

DISCUSSION AND FUTURE WORK

This work demonstrated the feasibility of a power composite, a structural material that harvests energy from ambient vibrations. Most importantly, we have shown that the power output of the piezoelectric tubes is compatible with the input requirements of the power fiber battery, and that the analytic model is a good predictor of structural response and electrical output for a given vibration environment.

Further development of the power composite components and packaging is necessary. The current fiber battery encapsulation technique produces end caps that are larger than the inside diameter of the piezo fibers. To fully integrate the energy generation and storage functions of the power fiber, we must either reduce the size of these encapsulated ends or fabricate the battery directly into the PZT tube. Figure 36 shows a fiber battery (from which the endcap has been removed) inserted into a copper-plated PZT tube.

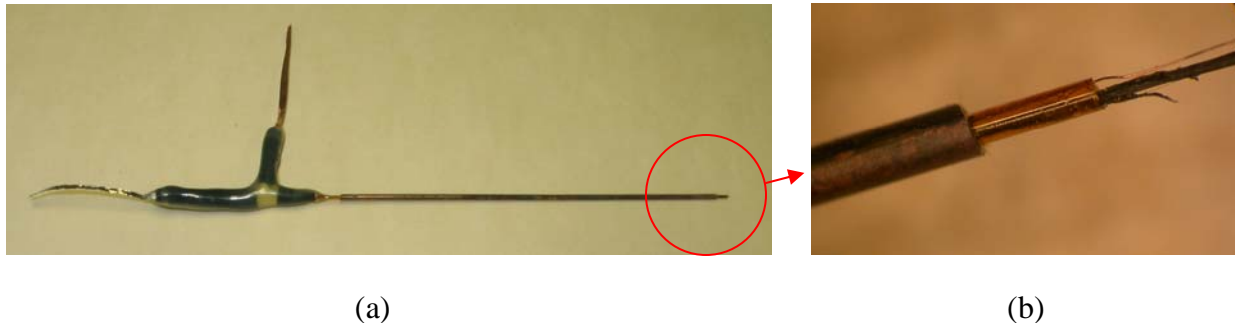


Figure 36. Fiber battery inserted into PZT tube.

SRI's new technique for electroding and poling the inner and outer wall surfaces of the PZT tubes has proven to be viable. However, the process will need to be improved to increase electrode thickness uniformity and production throughput for longer tubes. The analytic harmonic oscillation and PZT output model has been shown to successfully predict the tip displacement and output voltage for a three-layer bender with integrated PZT tubes. This model may now be used to customize the design of PZT benders for specific applications with unique vibration environments. The beam dimensions, number of piezoelectric tubes, and battery characteristics may be adjusted to achieve the desired frequency response, output voltage, charge time, and battery output for the application. This design tool may now be adapted to assess more complex structures than the simple cantilever beam of our recent work, and to potentially predict the structure-morphing capability of the multifunctional material characteristics of the power fiber.

A power composite needs to be made. Its power properties and structural response need to be tested. Measured results need to be compared with the model. Manufacturability issues need to be addressed, perhaps by discussions with composite producers.

REFERENCES

1. Shockey, D. A., Narang, S., Ventura, S. C., Simons, J. W., and Peterson, B. D., Battery Fibers for Composites and Textiles, Interim Progress Report submitted to the U. S. Army Research Office by SRI International, Contract No. DAAD19-00-C-0098, July 22, 2002.
2. Shockey, D. A., Narang, S., Ventura, S. C., Simons, J. W., and Peterson, B. D., Battery Fibers for Composites and Textiles, Annual Progress Report submitted to the U. S. Army Research Office by SRI International, Contract No. DAAD19-00-C-0098, April 25, 2004.